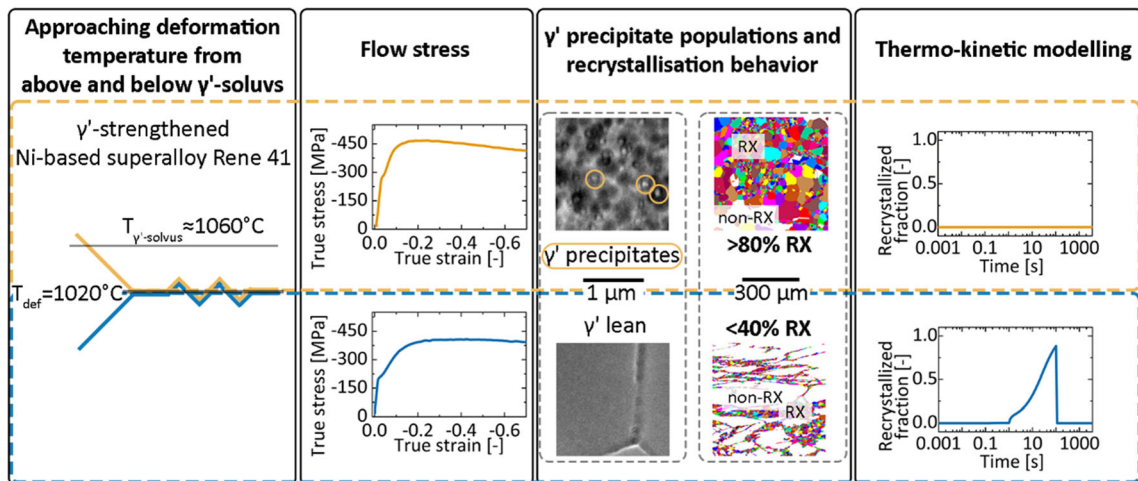


# Investigation and Simulation of the Effects of nm-Scale $\gamma'$ Precipitates on the Recrystallization of Ni-based Superalloys



R. BUERSTMAYR, F. THESKA, E. KOZESCHNIK, R.F. WEBSTER, M. LISON-PICK, S. STREET, and S. PRIMIG

Superalloys are critical materials for the hottest sections of stationary gas turbines and aircraft engines. Homogeneously fine-grained microstructures are essential to unlock their superior high-temperature strength but are challenging to achieve in  $\gamma'$ -containing Ni-based superalloys. Such microstructures are achieved by recrystallization through hot working and grain boundary pinning *via*  $\mu\text{m}$ -scale second phase particles. Discontinuous dynamic recrystallization is the predominant restoration mechanism, where grain growth is restricted by Zener pinning. Nanometer-scale  $\gamma'$  precipitates may exercise similar pinning during the nucleation stage and thus delay recrystallization. While the effects of coarse,  $\mu\text{m}$ -scale, precipitates during recrystallization and grain growth are well-known, descriptions for fine coherent precipitates are currently lacking. To address this scarcity of knowledge, both  $\gamma'$ -rich and -lean microstructures of the  $\gamma'$ -containing Ni-base superalloy René 41 underwent identical uniaxial hot compression tests. Flow stress and microstructural analyses reveal the inhibition of recrystallization by nm-scale  $\gamma'$  precipitates during both nucleation and growth stages. This effect is successfully described using thermo-kinetic modeling through application of a driving-force based model. These unique insights provide a novel pathway to unlock homogeneously fine-grained microstructures in  $\gamma'$ -containing Ni-based superalloys *via* advanced thermo-mechanical processing routes, required for applications in future generations of gas turbines and aircraft engines.



R. BUERSTMAYR, F. THESKA, and S. PRIMIG are with the School of Materials Science, & Engineering, UNSW Sydney, Kensington, NSW 2052 Australia. Contact e-mail: s.primig@unsw.edu.au E. KOZESCHNIK is with the Institute for Materials Science and Technology, TU Wien, Vienna 1060, Austria. R.F. WEBSTER is with the School of Materials Science & Engineering, UNSW Sydney and also with the Electron Microscope Unit, UNSW Sydney, Kensington, NSW 2052, Australia. M. LISON-PICK and S. STREET are with the Western Australian Specialty Alloys, Canning Vale, WA 6155, Australia.  
Manuscript submitted September 13, 2022; accepted February 5, 2023.  
Article published online March 3, 2023

<https://doi.org/10.1007/s11661-023-07008-w>  
© The Author(s) 2023

## I. INTRODUCTION

CAST and wrought Ni-based superalloys are the materials of choice for intermediate to high temperature components exposed to high dynamic loads and aggressive chemical environments.<sup>[1]</sup> Ni-based superalloys

have evolved into one of the most complex material classes in use today because of requirements to balance high-temperature strength, toughness with well as creep and corrosion resistance<sup>[1]</sup>. Having been developed in the 1950s and 60s, interest in the superalloy René 41 has recently spiked, as it exhibits exceptional high-temperature strength and fatigue properties required for future generations of more fuel-efficient aircraft engines.<sup>[2]</sup> However, its tendency to cracking and formation of inhomogeneous microstructures during thermo-mechanical processing remains a major challenge for manufacturers.<sup>[3,4]</sup> These challenges will need to be overcome to facilitate more widespread utilization of the excellent property profile of René 41 and similar alloys. To unlock their full potential, the microstructural evolution must be carefully controlled during thermo-mechanical processing, as grain size and grain boundary characteristics impact key material parameters such as hot workability<sup>[1,2,5]</sup> and mechanical properties of engineering parts.<sup>[1,5]</sup>

During thermo-mechanical processing, the following restoration mechanisms are generally accepted to be the most prevalent in superalloys: Dynamic recrystallization (DRX), post-dynamic recrystallization (PDRX) and static recrystallization (SRX).<sup>[1,2,6,7]</sup> Concurrent with recrystallization, dislocation annihilation may take place both as dynamic recovery (DRV) as well as static recovery (SRV).<sup>[8]</sup> In Ni-based superalloys, DRX is reported frequently.<sup>[2]</sup> PDRX effects in superalloys have first been reported by Sakai *et al.*,<sup>[9,10]</sup> and have found increasing focus in more recent studies on superalloy hot workability.<sup>[6,11,12]</sup> DRX is further subdivided in two mechanisms—continuous dynamic recrystallization (CDRX) and discontinuous dynamic recrystallization (DDRX). In CDRX, recrystallization occurs by the migration of subgrain boundaries and their gradual evolution into high angle grain boundaries, as well as the coarsening of the associated cell structure.<sup>[8]</sup> In DDRX, strain induced boundary migration leads to bulging of high angle grain boundary segments. Recrystallization nuclei are then formed from such bulged segments by accumulation of dislocations or twinning.<sup>[8,13]</sup> This latter mechanism is generally accepted to best represent recrystallization in low stacking fault face-centered cubic (FCC) materials such as Ni-base superalloys.<sup>[1]</sup>

The microstructure of René 41 consists of the FCC  $\gamma$ -matrix and predominantly nm-scale, fine intragranular  $\gamma'$  precipitates making up to 30 vol pct which provide the main contribution to the overall yield strength.<sup>[4,14]</sup> Other precipitates in René 41 are coarser intragranular M(C,N) carbonitrides and intergranular  $M_6C$  and  $M_{23}C_6$  carbides, all of which occur in comparably low volume fractions.<sup>[4,15,16]</sup> Homogeneous, fine-grained microstructures can be achieved by means of thermo-mechanical processing. This leads to refinement by recrystallization, afterwards grain growth is controlled *via*  $\mu\text{m}$ -scale second phase particles, leading to pinning of high- and low angle grain boundaries.<sup>[8,17]</sup> This is commonly described by the well-known Zener equation, relating volume fractions and radii of second phase particles to the final grain size.<sup>[17]</sup> This is a driving

force based model for grain growth, which includes terms accounting for energy stored in the microstructure in the form of dislocations and in high angle grain boundaries, as well as growth inhibiting pinning forces exerted by second phase particles.<sup>[8]</sup> However, this pinning effect of nm-scale precipitates may inhibit both, the nucleation and growth of recrystallized grains.<sup>[17]</sup> Here, a criterion for the inhibition of recrystallization has been formulated by Rollett *et al.*,<sup>[8,18]</sup> and in a similar form by Hillert.<sup>[19]</sup> It is based on the assumption that fine precipitates in the microstructure may hinder the conversion from low to high angle grain boundaries during CDRX.<sup>[8,20]</sup> As this is distinctly different from DDRX, which is generally accepted to be the dominant recrystallization mechanism in superalloys, the applicability of this model is on superalloys yet to be tested.<sup>[1,7,21]</sup>

Previous work on the effects of second phase particles during thermo-mechanical processing can be found for example in a study by Cremisio and McQueen.<sup>[22]</sup> However, the roles of precipitates and substructure evolution were only discussed briefly. Lizzi *et al.*<sup>[23]</sup> studied the hot deformation and recrystallization behavior of an Alloy 718 prototype. However, the temperature region chosen for this investigation was above the solvus temperatures for both the main hardening  $\gamma'$  and  $\gamma''$  phases, allowing only an evaluation of the incoherent incoherent  $\delta$  precipitates.<sup>[11]</sup> Comparing these results to other works on Alloy 718, it appears that these  $\delta$  phase precipitates do not have a large effect on the dynamic recrystallization behavior.<sup>[23]</sup> Nicolaÿ *et al.*<sup>[6]</sup> studied the effect of strain rate on the DRX and PDRX behavior in conventional Alloy 718 and found that increasing strain rates above  $0.1 \text{ s}^{-1}$  shifted the restoration behavior towards PDRX. Isothermal holding at temperatures above the  $\gamma'$  and  $\gamma''$  solvus temperatures of Alloy 718 led to a rapid PDRX response in materials deformed under such conditions.<sup>[6]</sup> Coyne-Grell *et al.*<sup>[24]</sup> studied interactions between recrystallization phenomena and  $\gamma'$  precipitates in the superalloy AD730. This work highlights the complexity, as they found that hetero-epitaxial recrystallization of coarse  $\gamma'$  precipitates can enhance recrystallization, while other forms of  $\gamma'$  precipitates can suppress it.<sup>[24]</sup> Zhang *et al.*<sup>[25]</sup> reported increased driving forces for DRX in the presence of  $\gamma'$  precipitates, while Nishimoto *et al.*<sup>[26]</sup> reported limited grain growth in the presence of coarse  $\gamma'$ , while recrystallization is promoted by high strains and high temperatures. In contrast, Seret *et al.*<sup>[27]</sup> found evidence that PDRX is not fully prevented by  $\gamma'$  precipitates *via* local dissolution and re-precipitation in proximity to the recrystallization front. Overall, the complex interaction of the PDRX behavior of Ni-based superalloys and the pinning effect by  $\gamma'$  precipitates is still not fully understood and requires additional exploration and further attention.

The aim of the current study is to relate the presence of nm-scale  $\gamma'$  precipitates to the flow stress and recrystallization of René 41 with focus on its PDRX behavior. To achieve this, carefully calibrated thermo-mechanical profiles were chosen to manipulate the  $\gamma'$  precipitate dispersion and its impact on flow stress and recrystallization. Isothermal holding after hot deformation, and

subsequent microstructural analysis then expand these insights to the PDRX behavior. Complementary thermo-kinetic modeling of the precipitation and deformation behavior using MatCalc<sup>[28,29]</sup> allows dynamic and post-dynamic recrystallization to be distinguished. The presented results provide a novel and unique approach to improve thermo-mechanical processing routes for homogeneously fine-grained microstructures in  $\gamma'$ -containing Ni-based superalloys for aircraft engine and gas turbine applications.

## II. MATERIALS AND METHODS

### A. Initial Microstructure and Heat Treatments

The material used in this study was provided by Western Australian Specialty Alloys (Perth, WA, Australia). A billet was produced *via* the standard production route of vacuum induction melting, followed by vacuum arc remelting at industrial facilities, followed by ingot-to-billet conversion at Overall Forge (Albury, NSW, Australia). The disk provided was 30 cm in diameter and 2.5 cm in thickness. An overview of the chemical composition provided in Table I was determined using X-ray fluorescence spectroscopy (XRF) and low-element combustion oxidation (LECO). Samples were taken from a position halfway between the center and the rim of the billet.

All samples were solution annealed at 1200 °C for 30 minutes followed by water quenching, to dissolve  $\gamma'$  precipitates as well as  $M_6C$  and  $M_{23}C_6$  precipitates. After this step, only the matrix and M(C,N) carbonitrides remained. Initial microstructural characterization was conducted and samples for hot deformation experiments were machined. Two batches of cylindrical samples were made. Larger samples with a length of 10 mm and a diameter of 8 mm were used for hot deformation at and above 1000 °C, and smaller samples with a length of 7.5 and a 6 mm diameter were used for hot deformation at 950 °C. Maintaining an identical height-to-diameter ratio of 1.25 allowed for reproducible hot deformation conditions.

### B. Hot Deformation Experiments

A Gleeble 3500 thermo-mechanical simulator was used for the hot deformation experiments. Type K thermocouples, spot welded to the cylindrical samples at their half height, were used to monitor and control the sample temperatures during the Gleeble experiments.

Two different thermo-mechanical profiles were applied prior to deformation. These will be referred to as ‘Type D’ (deformed) and ‘Type SD’ (solutionized and deformed) in the following, a qualitative plot is shown in Figure 1. The exact temperature and holding times are provided in Table II. In Type D, the target deformation temperature  $T_{def}$  was approached at 5 K s<sup>-1</sup>. The material was then held isothermally for 360 seconds, followed by uniaxial compression up to target true strain of  $\epsilon_{true} = 0.69$ , at a true strain rate of  $\dot{\epsilon}_{true} = 1$  s<sup>-1</sup>. For Type SD, an intermittent solutionizing temperature of 1150 °C was approached at 5 K s<sup>-1</sup>, followed by 30 seconds isothermal holding, to dissolve any retained  $\gamma'$  precipitates. Then,  $T_{def}$  was approached at 5 K s<sup>-1</sup>, followed by another isothermal holding period of 60 seconds prior to deformation. The material was deformed to identical  $\epsilon_{true}$  and  $\dot{\epsilon}_{true}$  as Type D. Due to adiabatic heating during plastic deformation, the heating current was turned off during deformation. For Type D and SD profiles, isothermal holding of 0, 36 and 360 seconds was carried out after deformation at 1000 °C and 1020 °C, while for deformation at 950 °C and 1100 °C only 0 seconds isothermal holding experiments were conducted.

The recorded flow stress data was corrected for friction based on the geometric measurements of the samples before and after deformation according to the approach proposed by Ebrahimi *et al.*<sup>[30]</sup> This approach indicated that the true flow stress was about 3 to 7 pct lower than the recorded flow stress, with the largest difference at the onset of deformation. The recorded peak flow stress was found to be about 5 pct lower after correction compared to the recorded raw data. A micrometer screw gauge was used to record the geometric data of the samples before and after testing. A locally estimated scatterplot smoothing function with a range of 0.025 was applied to reduce the noise in all the recorded flow stress curves using OriginPro (2018 version).

### C. Sample Preparation

After the uniaxial hot compression experiments, the samples were cut parallel to the loading direction across the center using SiC cutting disks, and hot mounted in resin. This was followed by standard metallographic preparation of grinding and polishing. The half samples intended for Electron Back-Scattered Diffraction (EBSD) were then unmounted for electrolytic polishing using a Struers LectroPol-5. This was done using an A2

Table I. Composition of René 41 as Used in this Study

	Element										
	Ni	Cr*	Co*	Mo*	Ti*	Al*	Fe*	C**	B*	N*	Residual***
At. Pct	bal.	20.59	10.79	5.75	3.80	3.29	1.31	0.276	0.033	0.015	0.23
Wt Pct	bal.	18.51	11.00	9.55	3.15	1.54	1.27	0.057	0.006	0.004	0.20

The elements summarized under ‘residual’ include Zr, W, Nb, O, Cu, V, Mn, Mg, S, Si and P\* Determined by XRF and \*\*determined by LECO the elements summarized under ‘residual’ include Zr, W, Nb, O, Cu, V, Mn, Mg, S, Si and P.

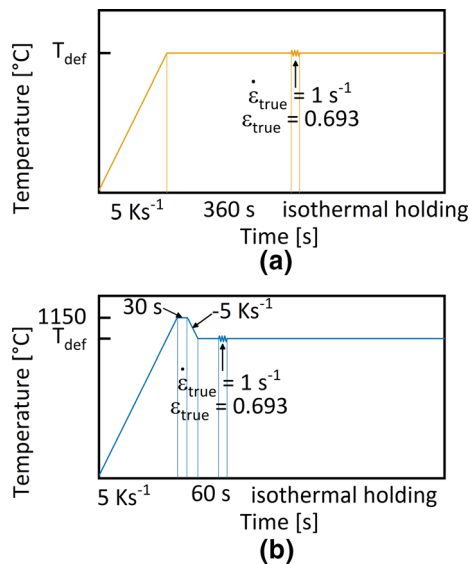


Fig. 1—Time-temperature-deformation plots for the two heat treatment profiles Type D (a) and Type SD (b) as in the described uniaxial compression tests.

**Table II. Target Deformation Temperatures, with Post-deformation Isothermal Holding Times as Applied During the Uniaxial Compression Tests**

$T_{\text{def}}$ [°C]	Isothermal Holding Time [seconds]		
950	0	—	—
1000	0	36	360
1020	0	36	360
1100	0	—	—

electrolyte under a potential of 20 V for 10 seconds at ambient temperature. The flow rate was adjusted to values ranging from ‘8’ to ‘12’. The other half of the samples were also prepared using standard metallographic methods but followed by electrolytic etching. This etching process initially follows the electrolytic polishing program, but is then followed by an additional etching step at 6 V for 20 seconds.

Samples deformed at 1020 °C with 0 seconds isothermal holding were selected for transmission electron microscopy (TEM) studies. These were prepared using standard focused ion beam (FIB) *in situ* lift-out techniques.<sup>[31]</sup> A ThermoFisher Helios G4 Xe plasma-FIB (PFIB) and a FEI Nanolab Ga FIB were used. Initial trenching and lift-out was performed on the PFIB operated at 30 kV with a probe current of 15 nA and cleaning cross sections were performed on the Ga FIB with a final probe current of 0.03 nA with a final low energy 5 kV polish to remove surface amorphization.

#### D. Microstructural Characterization

Scanning Electron Microscope (SEM) micrographs were recorded using a Zeiss Auriga CrossBeam workstation. All SEM micrographs presented here were

generated using a backscattered electron detector (NTS-BSD), at a working distance of 10 mm, an acceleration voltage of 15 kV and an aperture of 30  $\mu\text{m}$ . The scanning speed of the presented images was set to ‘8’. The FIJI ImageJ (version 1.53) software package was used to evaluate the  $\gamma'$  precipitate size distributions where they could be resolved *via* regular SEM.<sup>[32]</sup> Deep etched images exhibited high local contrasts, therefore a simple thresholding operation was insufficient for precipitate analysis. Due to the small size and large number of particles, a manual evaluation was deemed not feasible. Therefore, the trainable WEKA segmentation plugin available for FIJI ImageJ was used.<sup>[33]</sup> The WEKA plugin contains a machine learning feature for image analysis. Based on a manually selected training input, the software then develops a classification filter which can identify similar characteristics in an image. For a more detailed explanation, the reader is referred to the publicly accessible WEKA code, as well as the accompanying publication by the developers of WEKA.<sup>[33,34]</sup> This classification was used to Training of the analysis algorithm was conducted on a 1  $\mu\text{m}^2$  square subsection of the respective image with precipitates and matrix being manually indicated on the subset. The algorithm was then trained using the random forest model, until the ‘out of bag’ error reached a level of below 2 pct. This algorithm was then applied to the complete dataset.<sup>[33]</sup>

EBSD maps were generated using a JEOL 7001 SEM. All maps were collected using an acceleration voltage of 20 kV, a beam current of 12 nA and a working distance of 15 mm at a tilt angle of 70 deg. The maps were collected of an area of 600  $\times$  600  $\mu\text{m}^2$  with a step size of 0.5  $\mu\text{m}$ . An EDAX Hikari Super camera system was used with a binning factor of 8  $\times$  8 at 300 to 400 fps and a gain values ranging from 450 to 550. Phases included the standard fcc nickel with a lattice parameter of 3.56 Å to evaluate the matrix and a B2-ordered TiC with an adapted lattice parameter of 4.6 Å to detect M(C,N) carbonitrides. Other phases, such as  $\text{M}_{23}\text{C}_6$  and  $\text{M}_6\text{C}$ , were not recorded due to their small size relative to the selected step size. All analysis and clean-up operations were conducted using the TSL OIM suite (version 7.9.9.6). The clean-up operations applied to the maps were a confidence index (CI) standardization (settings 5 deg misorientation, grains have a minimum size of 5 datapoints), a confidence index correlation clean-up, cleaning up all datapoints with CI < 0.1, and a phase correlation clean-up for datapoints with CI < 0.2. To remove mis-indexed regions consisting of 1 to 2 deg datapoints, a grain dilation clean-up with 5 deg misorientation and a minimum grain size of 3 datapoints was added. The last step was a Kuwahara-orientation smooth with a Kernel radius of 2 nearest neighbors. After the clean-up operations, two partitions were created from each entire dataset. The first partition contained grains with a grain orientation spread (GOS)  $\leq$  2.5 deg as grains within this range were assumed to be recrystallized. The second partition contained grains with a GOS > 2.5 deg, i.e. deformed grains that had not undergone recrystallization. This GOS cut-off value of 2.5 deg was determined empirically

based on the GOS distribution observed in the data. An example of such a GOS distribution, with the cutoff value indicated can be seen in the electronic supplementary file, in Figure S1. As can be seen, the cutoff value is close to a minimum in the number fraction of grains observed. This value is also similar compared to other works on superalloys, such as in References 23, 35. After the generation of these partitions, a correction for primary  $\Sigma 3$  and secondary  $\Sigma 9$  twin boundaries was applied before evaluation of the grain size of recrystallized and deformed fractions, respectively. Furthermore, a geometrically necessary dislocation (GND) density evaluation of the fraction with a GOS  $> 2.5$  deg was conducted. This evaluation was applied as implemented in the TSL OIM suite, assuming a Burger's vector of 0.252 nm. Maps were generated and the average GND was evaluated for a GND density of up to  $1000 \times 10^{13} \text{ m}^{-2}$ . Histograms of the GND density distribution were evaluated using OriginPro (2018 version), fits were generated assuming a log-normal distribution. The reported values correspond to the median of the fitted distribution, errors to the standard deviation.

TEM micrographs were collected using a JEOL - JEM-F200 TEM operated at 200 kV with a Gatan One-View 4kx4k CMOS camera. Dark-field micrographs were collected after tilting the samples into a  $\mathbf{g} = [200]$  two-beam condition where  $\mathbf{g}$  is the diffraction vector.<sup>[31]</sup> The densities were then measured using the line-intercept method, where a series of random lines of total length  $l$  are drawn onto the micrograph, counting the number  $n$  of intersecting dislocations.<sup>[36]</sup> Convergent beam electron diffraction (CBED) patterns of the foils were collected. CBED patterns were then simulated over a thickness range of 3 to 300 nm in 3 nm steps, with the closest match to the experimentally generated pattern being used to evaluate the foil thickness  $t$ .<sup>[31]</sup> The total dislocation density was then calculated according to  $\rho = 2n/lt$ .<sup>[36]</sup>

### E. Thermo-kinetic Modeling

Thermo-kinetic modeling of the phase and microstructural evolution during hot deformation was achieved using MatCalc (version 6.04, release 0.123).<sup>[28,37]</sup> The chemical composition was chosen as in Table I. The elements summarized as 'rest' are ignored to simplify the system. This reduces the computational expense of the system. Further, there is often insufficient thermodynamic data available in the investigated range to provide useful insight. For example, there is no thermodynamic data at all included for  $P$ , while the database contains no consideration for the solubility of Cu in  $\gamma'$ .<sup>[38]</sup> It can be expected that some of these elements may slightly modify the solvus levels of individual phases due to their low presence of a total of 0.2 wt pct and the aforementioned insufficient thermodynamic data. However, it was deemed more accurate not to include them. The phases included in the simulations are:

- The FCC- $\gamma$  matrix,
- the primary Ti-rich M(C,N) carbonitrides, which were set up as a pre-existing precipitate,

- $\gamma'$  as homogeneous precipitates, and
- $M_6C$  and  $M_{23}C_6$  as grain boundary precipitates.

Exemplary simulated heat treatment and deformation profiles match the initial solution anneal and water quenching step, followed by those described as Type D and Type SD in Figure 1. Simulated true strains are increased to  $\varepsilon_{\text{true}} = 1.0$ , with a strain rate of  $\dot{\varepsilon}_{\text{true}} = 1.0 \text{ s}^{-1}$ , respectively. This was done to compensate friction induced effects leading to increased strains in the center of uniaxial compression samples.<sup>[30,39]</sup> The dislocation evolution in the material was approximated using a Kocks–Mecking-type approach to describe dislocation generation and annihilation, with rate equations describing dislocation generation, as well as dynamic and static recovery.<sup>[28,40–43]</sup> The principle of similitude is applied to describe the subgrain evolution.<sup>[28,43]</sup> The grain size was described using the MatCalc multi-class model, with the grain size development described in References 44. The initial grain size distribution was set to match a log-normal distribution with mean grain diameter of  $\sim 200 \mu\text{m}$ . The initial M(C,N) carbonitride phase fraction was set to be equal to the equilibrium phase fraction at 1200 °C as predicted for the present composition by MatCalc. A precipitate distribution of M(C,N) carbonitride particles was then generated, ranging in size from 500 to 2000 nm, and a total phase fraction equal to the equilibrium phase fraction predicted at 1200 °C, approximating the initial microstructure. Recrystallization was simulated with the standard pre-set parameters implemented in MatCalc. Where possible, the substructure parameters were further improved using, (i) a Read–Shockley model of substructure description,<sup>[45]</sup> (ii) a dislocation density dependent approximation of the misorientation angle between subgrains between 0 and 5 deg,<sup>[43,46]</sup> (iii) the Young's modulus according to experimentally generated data,<sup>[47]</sup> and (iv) the Burger's vector according to experimentally generated data at room temperature, corrected for crystallographic thermal expansion.<sup>[48,49]</sup> The pinning strength of the  $\gamma'$  precipitates was increased by a factor of 2, to account for their coherent nature.<sup>[1,17]</sup> For the script used to generate the presented results please refer to the electronic supplementary file as Script SC1. This file also contains the complete set of all input parameters for the simulation setup.

## III. RESULTS

### A. Initial Microstructure

The initial solutionizing heat treatment at 1200 °C for 30 minutes led to an initial microstructure with a mean grain radius of  $165 \pm 122 \mu\text{m}$ , and an M(C,N) carbonitride volume fraction of approximately  $0.5 \pm 0.2$  vol pct, as revealed by an initial EBSD evaluation. Exemplary micrographs of this microstructure can be seen in Figure 2. M(C,N) carbonitrides are pointed out by arrows in Figures 2(a) and (b). Grain boundaries shown in Figure 2(b) were found to be free of precipitates according to SEM imaging. For a better illustration of

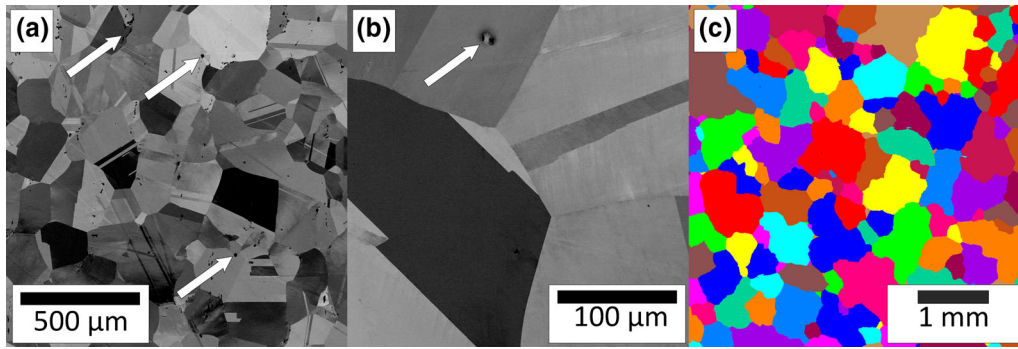


Fig. 2—Microstructure of the as received René 41 after the initial heat treatment of 1200 °C for 30 min followed by water quenching. Arrows point out M(C,N) type carbonitrides (a) Overview to show the overall grain structure and size. (b) Detail showing the precipitate-free grain boundaries. (c) EBSD unique grain color map (Color figure online).

the grain size, a EBSD unique grain color map is provided in Figure 2(c).

### B. Hot Deformation Behavior

Figure 3 shows the influence of profiles Type D and SD on the flow stress evolution. Note that the values for true stress and true strain presented here have negative signs due to the deformation experiments being executed in compression mode. No significant differences in stress were observed when deforming the material at 950 °C, as can be seen in Figure 3(a). For deformation at 1000 °C and 1020 °C, Type D resulted in a maximum stress of up to 625 MPa and 470 MPa, respectively, which was significantly higher than the observations for Type SD of up to 450 MPa and 400 MPa, respectively. This effect was most pronounced at 1000 °C in Figure 3(b), where at a true strain of  $-0.2$  the value of flow stress of Type D increased by  $\sim 175$  MPa. At 1020 °C, as seen in Figure 3(c), Type D exhibited an increase of  $\sim 70$  MPa at a true strain of  $-0.2$  relative to Type SD. This correlated to the temperature range where only Type D samples were expected to contain  $\gamma'$  precipitates. Three equivalent flow stress curves at 1000 °C and 1020 °C were recorded for both Type D and SD programs respectively, with only the following isothermal holding periods varying after the deformation was complete. These datasets show a high reproducibility of the deformation behavior at 1000 °C and 1020 °C and are provided in supplementary Figures S2 and S3. At 1100 °C, as displayed in Figure 3(d), the flow stress curves did not exhibit any significant differences.

### C. Microstructural Evolution

Figure 4 shows the evolution of the microstructure after hot deformation profile Type D at  $T_{\text{def}} = 1020$  °C, after 0, 36 and 360 seconds isothermal holding. Figures 4(a) through (c) show GOS maps from 0 to 2.5 deg in grey scale, respectively. Immediate quenching and 36 seconds isothermal holding resulted in similar appearances with low recrystallized volume fractions of 2 and 5 vol pct respectively. After 360 seconds isothermal holding, the recrystallized fraction as well as size of

recrystallized grains observed were significantly larger. Grain boundaries ranging from 5 to 15 deg misorientation are shown in green, high angle grain boundaries with a misorientation  $> 15$  deg in red, and the special grain boundaries  $\Sigma 3$  and  $\Sigma 9$  in red, while M(C,N) carbonitrides are shown in yellow. A quantitative evaluation of the grain boundary fractions in Figure 4 shows that after 0 and 36 seconds isothermal holding the misorientations from 5 to 15 deg are 2.63 and 4.57 cm respectively, which drops to 0.59 cm after 360 seconds of isothermal holding. The evolution of high angle grain boundaries on the other hand starts at levels of 2.76 cm, increasing to 5.08 cm after 36 seconds and 9.36 cm after 360 seconds. The length of  $\Sigma 3$  and  $\Sigma 9$  grain boundaries is 0.33 cm and 0.72 cm after 0 and 36 seconds isothermal holding and increases to 3.34 cm after 360 seconds. Figures 4(d) through (f) show unique grain color maps for the recrystallized fractions. Deformed areas are shown in white and represent non-recrystallized areas, areas shown in black are M(C,N) carbonitrides. The formation of necklace structures becomes obvious in this representation. For hot deformation at  $T_{\text{def}} = 1000$  °C, comparable maps are provided in supplementary Figure S4.

Figure 5 provides the corresponding dataset to Figure 4, except for the thermal history prior to deformation corresponding to a Type SD heat treatment. The same GOS cut-off value of 2.5 deg leads to a similar appearance after immediate quenching in Figures 5(a) and (d), with the recrystallized material exhibiting small volume fractions and grain sizes. However, isothermal holding of 36 seconds leads to pronounced recrystallization as seen in Figures 5(b) and (e). After 360 seconds, almost the entire microstructure consists of recrystallized grains, with a much larger mean grain size, as shown clearly in Figures 5(c) and (f). The length of grain boundary elements evolves from 2.26 to 0.25 and then 0.21 cm for the misorientations between 5 and 15 deg from 0 to 36 seconds and then 360 seconds isothermal holding. The length of high angle grain boundaries increases from 0.48 to 3.03 cm and 3.53 cm from 0 to 36 seconds and 360 seconds isothermal holding. Similarly, the length of  $\Sigma 3$  and  $\Sigma 9$  grain boundaries increases from 0.53 to 3.15 cm and

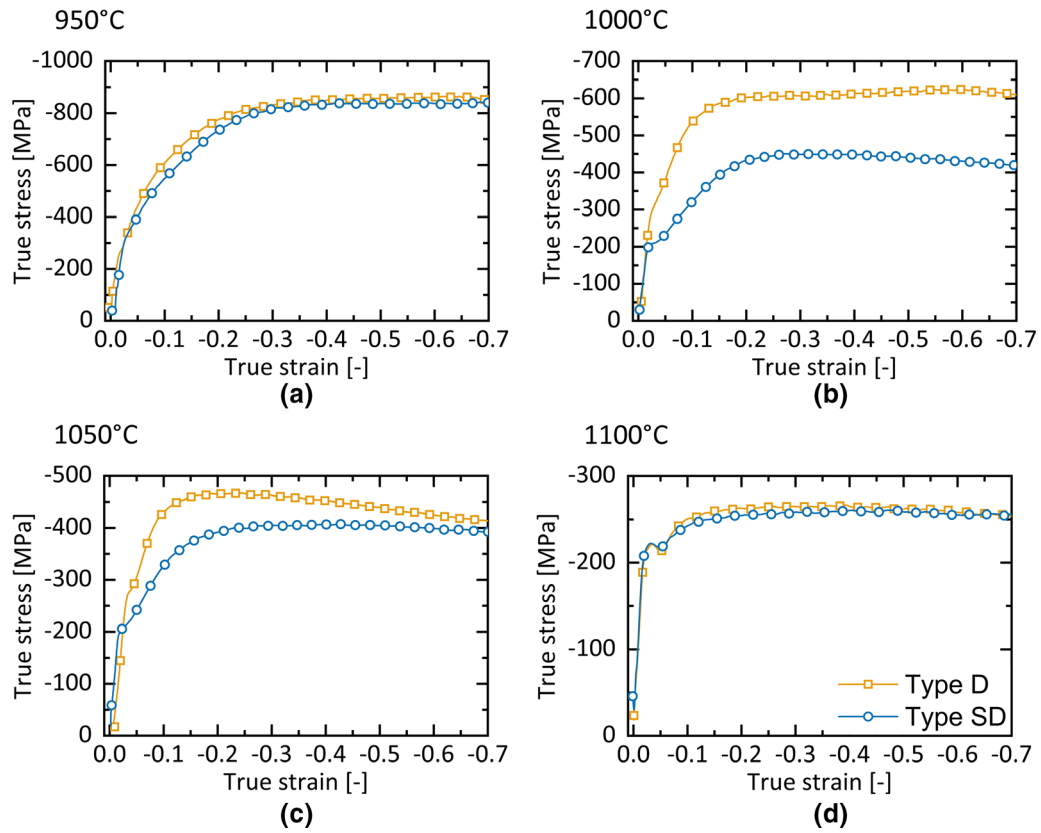


Fig. 3—Flow stress curves for Type D and SD thermo-mechanical profiles at different deformation temperatures. (a) at 950 °C, Type D and SD profiles show no significant differences, (b) and (c) at 1000 and 1020 °C, Type D exhibits significantly increased flow stress at  $-0.2$  true strain, and (d) 1100 °C, Type D and SD profiles show no significant differences.

3.63 cm over the same time scale. A comparable figure for Type SD heat treatments and deformation at 1000 °C is provided in the supplementary Figure S5.

Figure 6 shows mean diameters and volume fractions of those grain fractions with a GOS < 2.5 deg from Figures 4 and 5. In the Type D profile, the mean grain diameter and volume fraction of the recrystallized material did not increase significantly between 0 and 36 seconds isothermal holding increasing only from  $3.3 \pm 2.0 \mu\text{m}$  and 2.1 vol pct to  $2.7 \pm 1.3 \mu\text{m}$  and 5.1 vol pct. Only after 360 seconds isothermal holding significant recrystallization was observed at a recrystallized grain size of  $11.1 \pm 5.8 \mu\text{m}$  and a fraction of 36.3 vol pct. Comparatively, Type SD profiles led to a more rapid response after 36 s, with grain diameters and volume fraction increasing from  $2.5 \pm 0.9 \mu\text{m}$  and 13.3 vol pct to  $19.8 \pm 11.1 \mu\text{m}$  and 50 vol pct, respectively. After 360 seconds, the grain diameter and volume fraction approach  $43 \pm 27.8 \mu\text{m}$  and 87.8 vol pct. No changes in the M(C,N) carbonitrides were observed, with fractions of  $0.5 \pm 0.3$  vol pct for all generated datasets. An equivalent plot describing evolutions of grain sizes and recrystallized fractions after deformation at 1000 °C can be found in the supplementary Figure S6.

In addition to these results, GND density maps are shown in Figure 7 for the Type D and SD profile at 1020 °C. The maps in Figures 7(a) and (c) reveal that

the average GND density started high in both the Type D and SD profiles, with measured values corresponding to  $197 \pm 276 \times 10^{13}$  and  $196 \pm 306 \times 10^{13} \text{ m}^{-2}$ , respectively. After 36 seconds of isothermal holding, the GND density observed in Figure 7(c) corresponding to the Type D profile did not change noticeably, while the GND density in Figure 7(e) shows that in the Ty390pe SD profile the GND density decreased, with measured values corresponding to  $350 \pm 585 \times 10^{13}$  and  $63 \pm 57 \times 10^{13} \text{ m}^{-2}$ , respectively. Figures 7(c) and (f) show that after 360 seconds isothermal holding time the GND density in both profiles decreased, with average values of  $110 \pm 124 \times 10^{13}$  and  $22 \pm 14 \times 10^{13} \text{ m}^{-2}$  respectively showing that the decrease was more pronounced in the Type SD profile. The large standard deviations are due to the measured values of GND density spanning several orders of magnitude, especially in the deformed states. The data in supplementary Figure S7 illustrates that the changes are clear despite these standard deviations. The standard deviations in the Type SD profile decrease faster and are overall smaller relative to the mean compared to the Type D profile. The white arrows in Figure 7 indicate regions of high dislocation densities, while the white bars correspond to the locations of line profiles used to evaluate the orientation gradient within deformed grains. Data for these orientation gradients is provided in the supplementary Figure S8, the measured

## Deformation program Type D - 1020°C

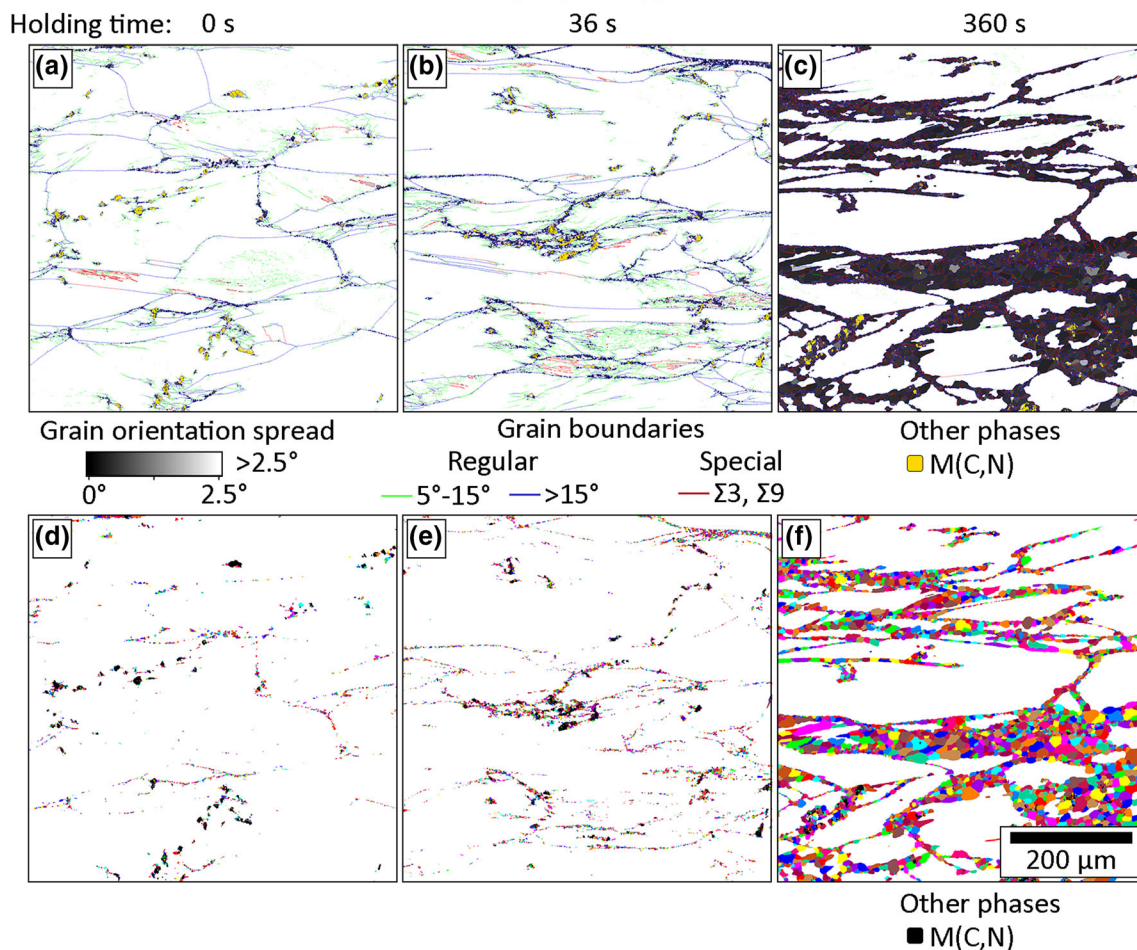


Fig. 4—Microstructural evolution after the hot deformation profile Type D at  $T_{\text{def}} = 1020\text{ }^{\circ}\text{C}$  and isothermal holding. (a) to (c) GOS maps in grey scale with grain boundaries with a misorientation of 5 to 15 deg in green, a misorientation of  $> 15$  deg in blue and the special  $\Sigma 3$  and  $\Sigma 9$  boundaries in red, while M(C,N) carbonitrides are yellow. Recrystallized grains are shown in grey and form necklace structures. (d) to (f) Unique grain color maps showing individual grains, areas of GOS  $> 2.5$  deg appear white and represent non-recrystallized grains, black areas represent M(C,N) carbonitrides. The isothermal holding times are 0 s (a, d), 36 s (b, e) and 360 s (c, f) (Color figure online).

orientation gradients correspond to ca.  $0.15\text{ deg }\mu\text{m}^{-1}$ . Equivalent GND density maps describing the development after deformation at  $1000\text{ }^{\circ}\text{C}$  are provided in supplementary Figure S9.

Concurrent to the GND results, TEM data on the dislocation density is provided in Figure 8. Figure 8(a) shows a dark-field micrograph and CBED pattern of a Type D sample deformed at  $1020\text{ }^{\circ}\text{C}$ , followed by 0 seconds of isothermal holding. The dislocation density in this sample was determined to be  $3.94 \pm 0.7 \times 10^{14}\text{ m}^{-2}$ . Figure 8(b) shows the same results for the corresponding Type SD sample, with a dislocation density of  $1.45 \pm 0.2 \times 10^{14}\text{ m}^{-2}$ .

No  $\gamma'$  precipitates were visible in any material after Type D and SD heat treatments for 0 seconds isothermal holding after deformation. However, when studying the material after the isothermal holding periods of 360 seconds, differences became apparent. Figure 9(a) shows a deep etched microstructure after a Type D program followed by deformation and 360 seconds of isothermal holding with a target deformation and

holding temperature of  $1020\text{ }^{\circ}\text{C}$ . The observed  $\gamma'$  precipitates were of a size of  $40 \pm 12\text{ nm}$  in radius and took up an overall fraction of approximately 3 vol pct. In the corresponding Type SD microstructure shown in Figure 9(b), after the same isothermal holding period at  $1020\text{ }^{\circ}\text{C}$ , no precipitates can be seen. This means that any  $\gamma'$  precipitates present are below the resolution limit of the SEM.

### D. Thermo-kinetic Modeling

The results from thermo-kinetic modeling in Figure 10 show the trends of recrystallization for Type D and Type SD profiles, while Figure 11 shows the corresponding evolution of  $\gamma'$  precipitates. As Figure 10(a) shows, deformation at  $950\text{ }^{\circ}\text{C}$  was not predicted to lead to significant recrystallization in both Type D and SD profiles. Figures 10(b) and (c) on the other hand show that a strong dependence of recrystallization at  $1000\text{ }^{\circ}\text{C}$  and  $1020\text{ }^{\circ}\text{C}$  with respect to the application of a Type D or SD profile was predicted.



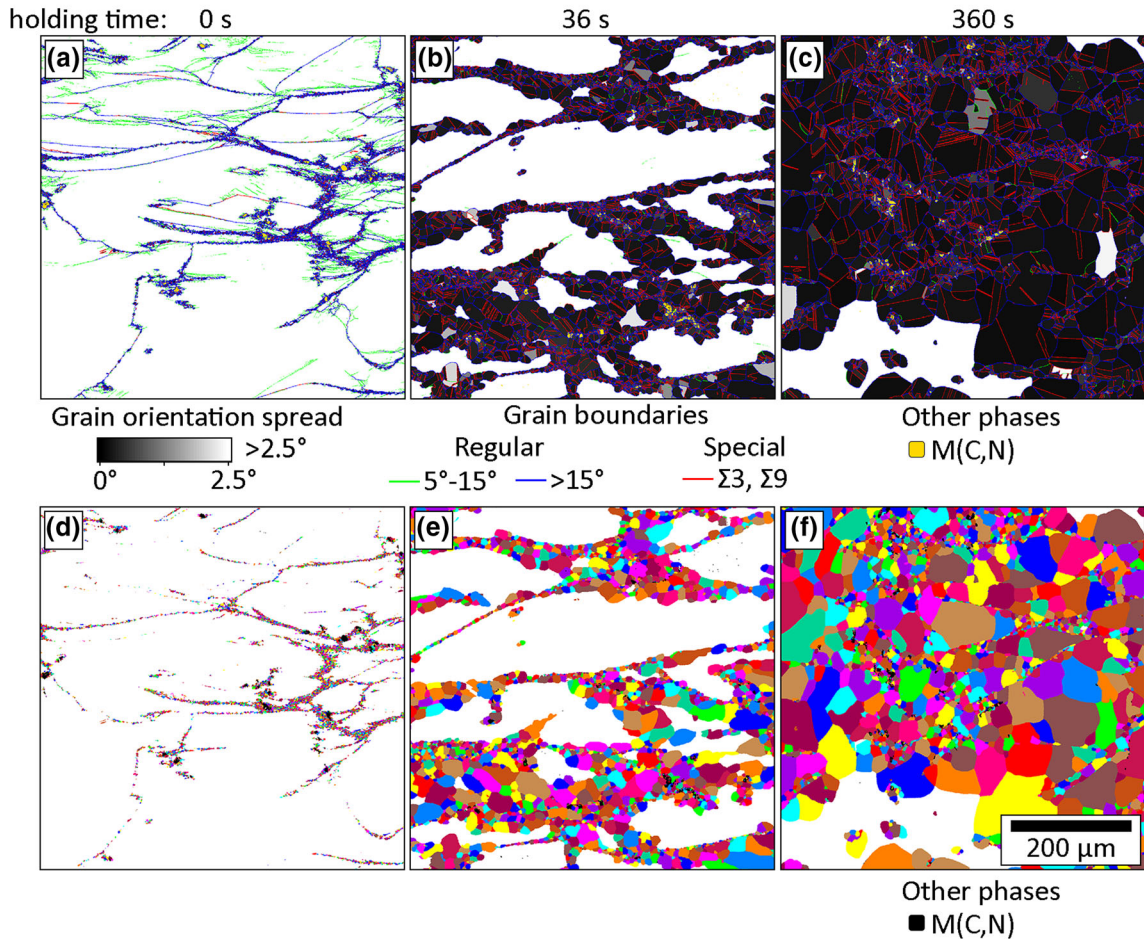


Fig. 5—Microstructural evolution after the hot deformation profile Type SD at  $T_{\text{def}} = 1020\text{ }^{\circ}\text{C}$  and isothermal holding. (a) to (c) GOS maps in grey scale with grain boundaries with a misorientation of 5 to 15 deg in green, a misorientation of  $> 15$  deg in blue and the special  $\Sigma 3$  and  $\Sigma 9$  boundaries in red, while M(C,N) carbonitrides are yellow. Recrystallized grains appear dark grey and form necklace structures. (d) to (f) Unique grain color maps showing individual grains, areas of GOS  $> 2.5$  deg appear white and represent non-recrystallized grains, black areas represent M(C,N) carbonitrides. The isothermal holding times are 0 s (a, d), 36 s (b, e) and 360 s (c, f) (Color figure online).

While Type D profile simulations led to almost no recrystallization, Type SD profiles led to pronounced recrystallization, mostly restricted to the times after the deformation is finished, which is indicated by the grey dashed line for all graphs displayed in Figure 10. In simulations at  $1100\text{ }^{\circ}\text{C}$ , above the  $\gamma'$ -solvus temperature of about  $1060\text{ }^{\circ}\text{C}$ ,<sup>[4]</sup> recrystallization occurred in either of the two thermal profiles applied as seen in Figure 10(d). This recrystallization too was predicted to predominantly occur after the deformation was completed (*i.e.* post-dynamic recrystallization).

Corresponding to the results of recrystallized and deformed volume fractions, the results for volume weighted  $\gamma'$  precipitate radii and phase fractions are presented in Figure 11. At  $950\text{ }^{\circ}\text{C}$ , the simulation results in Figure 11(a) predict  $\gamma'$  precipitates for both Type D and SD profiles, with similar fractions of around 15 mol pct predicted for both, while the radii in the Type D profile at approximately 50 nm were expected to be larger than those in Type SD with about 25 nm at the beginning of deformation, followed by coarsening to

roughly 30 nm after 360 and 50 nm after 3600 seconds of simulated isothermal holding post deformation. At  $1000\text{ }^{\circ}\text{C}$  and  $1020\text{ }^{\circ}\text{C}$ , as shown in Figures 11(b) and (c), there was no presence of  $\gamma'$  precipitates expected in Type SD profiles, while in Type D profiles around 8.5 and 5 mol pct, respectively, were predicted. At  $1100\text{ }^{\circ}\text{C}$ , no  $\gamma'$  precipitates predicted during any stage of the simulations, therefore, the respective graph is omitted here.

For phase fractions and radii of  $\text{M}_6\text{C}$  and  $\text{M}_{23}\text{C}_6$ , no significant changes during the simulations in both Type D and SD profiles were predicted. They are therefore not depicted in the graphs. Initial volume fractions and radii, depending on  $T_{\text{def}}$  are provided in Table III. These predicted radii are in the order of several 100 nm, with the fractions always below 1 mol pct for all results presented here.

The evolution of the predicted dislocation density with isothermal holding following thermo-mechanical profiles Types D and SD at  $T_{\text{def}} = 1020\text{ }^{\circ}\text{C}$  in Figure 12 predicted the highest dislocation densities immediately after deformation at 0 seconds of isothermal holding

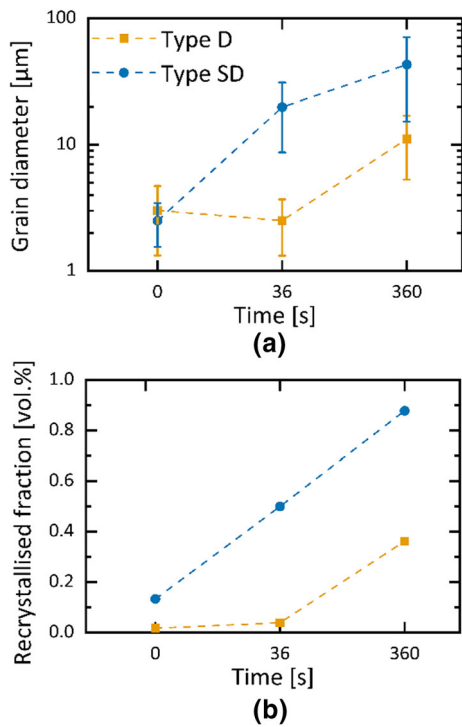


Fig. 6—(a) Volume weighted mean diameter of recrystallized grains for both profiles at  $T_{\text{def}} = 1020$  °C. The Type SD thermo-mechanical profile results in a more immediate increase of the recrystallized fraction and significantly larger grains after 360 s isothermal holding. Error bars represent standard deviations. (b) Recrystallized volume fractions of both profiles at  $T_{\text{def}} = 1020$  °C. Type SD results in a rapid increase to 87.8 vol pct after 360 s isothermal holding.

time. The situation is similar for both types of heat treatments, at  $1.01 \times 10^{14} \text{ m}^{-2}$  in the Type D and  $1.17 \times 10^{14} \text{ m}^{-2}$  in the Type SD profiles. After 36 seconds isothermal holding, the dislocation density decreased to  $1.15 \times 10^{13} \text{ m}^{-2}$  and  $6.8 \times 10^{12} \text{ m}^{-2}$  for Types D and SD, respectively. After 360 seconds isothermal holding, a further decrease to  $7.5 \times 10^{12}$  and  $5.6 \times 10^{11} \text{ m}^{-2}$  for Types D and SD respectively was predicted. The calculated dislocation density decreased more severely during isothermal holding for the Type SD profile. The recovery model applied in this simulation describes the dislocation density inside of the cells in the substructure. This correlated with the expected absence of  $\gamma'$  precipitates as shown in Figure 11(c). In return, the higher retained dislocation density during isothermal holding for Type D profile correlated with the presence of  $\gamma'$  precipitates. The equivalent data corresponding to simulated deformation at 1000 °C is provided in supplementary Figure S10.

#### IV. DISCUSSION

The combination of experimental results and thermo-kinetic modeling can now be used to discuss the impact of  $\gamma'$  precipitates on flow stress behavior and microstructural restoration processes. Based on these

complementary insights, models are applied to understand the observed pinning effects.

##### A. Thermal Profile vs Restoration Behavior

At 950 °C the flow stress data in Figure 3(a) reaches around 800 MPa, independently of Type D and SD profiles, respectively. This corresponds to the finding that  $\gamma'$  precipitates are expected to form independently of the thermal history, as evidenced by the simulation results in Figure 11(a). The flow stress results also match previous results for René 41.<sup>[3]</sup> DRV is reported to be the dominant restoration mechanism in Waspaloy, which is similar in composition and hardening behavior.<sup>[50]</sup> The similarities in the flow stress curves for Type D and SD profiles reveal that DRV is the main microstructural restoration mechanism at 950 °C. This is supported by thermo-kinetic modeling in Figure 10(a).<sup>[3,50]</sup>

At 1100 °C, well above the  $\gamma'$  solvus temperature of approximately 1060 °C,<sup>[4]</sup> the flow stress curves in Figure 3(d) are similarly independent of the thermo-mechanical profile. This indicates that the restoration behavior is similarly dominated by DRX, as confirmed by the simulation results from Figure 10(d). Predicted differences in  $\text{M}_6\text{C}$  and  $\text{M}_{23}\text{C}_6$  grain boundary carbides in Table III do not appear to have a significant influence on deformation and recrystallization.

At temperatures slightly below the  $\gamma'$  solvus temperature, at 1000 °C and 1020 °C, significant differences in flow stress are observable. Type D contains high volume fractions and large radii of  $\gamma'$  precipitates according to simulation results in Figures 11(b) and (c). The results are high flow stresses of 600 and 475 MPa at 1000 °C and 1020 °C (Figures 3(b) and (c)), respectively. This is significantly higher when compared to approximately 450 and 400 MPa in the  $\gamma'$ -lean Type SD profile. Similarly, works on Waspaloy by Utada *et al.*<sup>[51]</sup> found a marked decrease in strength when the material was rapidly overheated.

Studying the evolution of GND density as well as predicted dislocation densities in Figures 7 and 12 over time, a significantly faster and more severe drop in dislocation density is present in the Type SD profiles compared to the Type D profiles. This indicates that  $\gamma'$  precipitates strongly inhibit recovery, as reported on other superalloys previously.<sup>[1,50]</sup> A similar effect of  $\gamma'$  precipitates on PDRX is also apparent. In the  $\gamma'$ -rich Type D profile, recrystallization proceeds more slowly than in the  $\gamma'$ -lean Type SD profile (Figures 4 and 5). Thus,  $\gamma'$  precipitates affect both, the flow stress and microstructural restoration mechanisms. This is consistent with the simulation results in Figure 10, although the recrystallization in simulations of Type SD profiles is more rapid than experimentally observed. On the other hand, in the Type D profiles, almost no recrystallization is predicted, although 360 seconds of isothermal holding at 1020 °C leads to about 36 vol pct of recrystallized material.

The simulated data in Figure 12 and GND results from Figure 7 indicate that the dislocation density after deformation is at a similar level after deformation. The

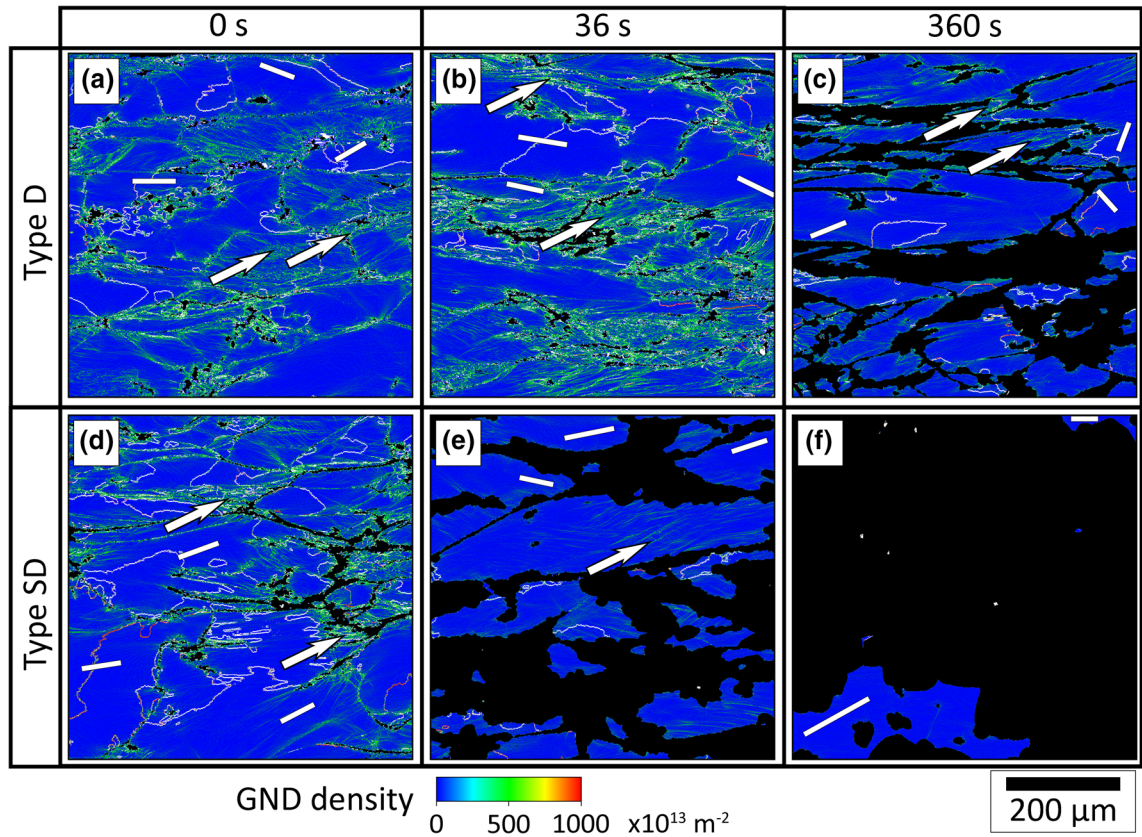


Fig. 7—GND density maps as evaluated based on EBSD data for the samples deformed after Type D (a), (b), (c) and Type SD (d), (e), (f) heat treatments at 1020 °C for the partition with a GOS < 2.5 deg. The isothermal holding times are 0 s (a), (d), 36 s (b), (e) and 360 s (c), (f). The arrows indicate areas of high dislocation density, the white bars represent lines along which orientation profiles were evaluated.

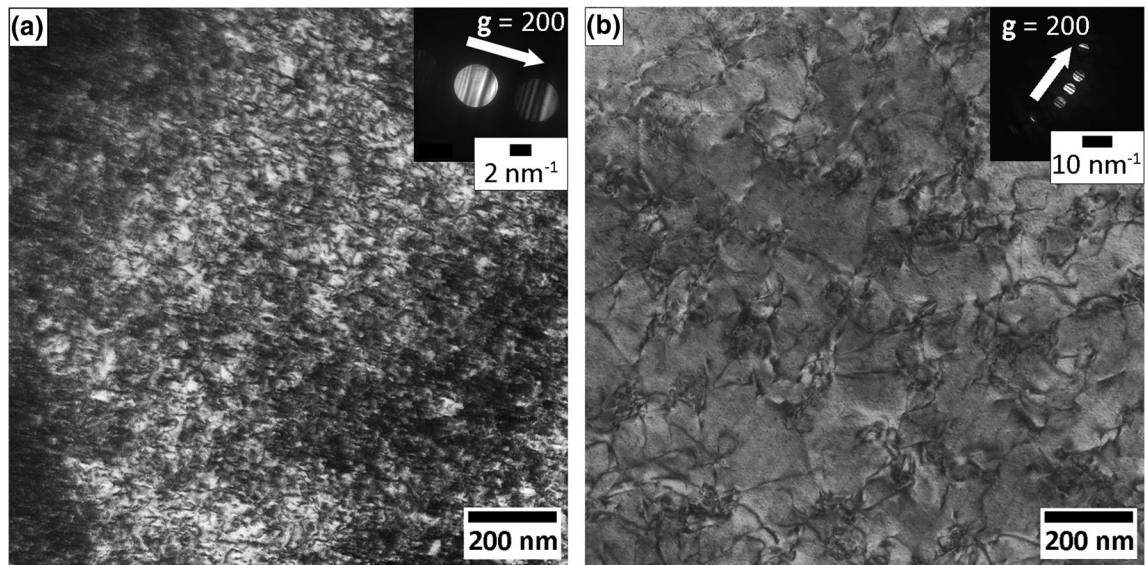


Fig. 8—TEM micrographs representing 2-Beam dark-field conditions and CBED patterns for a Type D sample for 0 s isothermal holding (a) and a Type SD sample for 0 s isothermal holding (b) after deformation at 1020 °C. The dislocation density is visibly higher in the Type D sample. The arrows next to the CBED pattern indicate the beam condition.

TEM studies show a difference in dislocation densities after deformation at  $3.94 \pm 0.7 \times 10^{14} \text{ m}^{-2}$  in the Type D and  $1.45 \pm 0.2 \times 10^{14} \text{ m}^{-2}$  in the Type SD profile

after 0 seconds of isothermal holding. These results do however still follow the qualitatively observed trend that the Type D samples exhibit a higher dislocation density

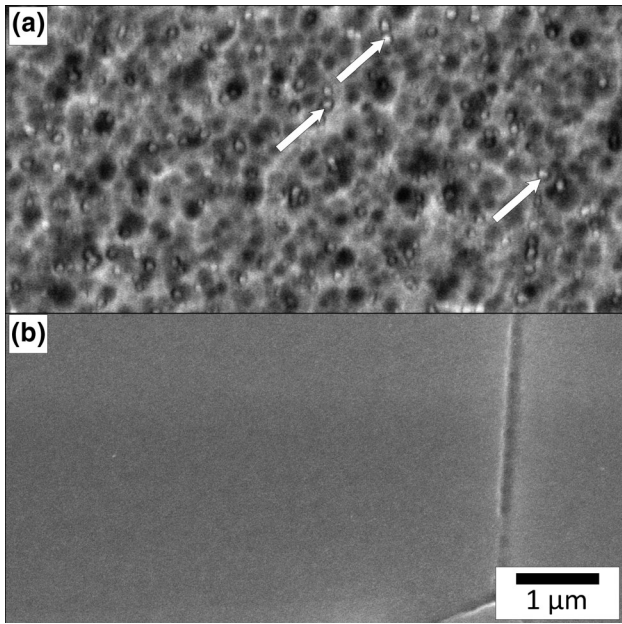


Fig. 9—SEM micrographs after deformation at 1020 °C followed by 360 s isothermal holding. The profiles prior to deformation are Type D, white arrows point out  $\gamma'$  precipitates (a) and Type SD, any present  $\gamma'$  precipitates cannot be resolved (b). The same scalebar applies to both micrographs.

than the Type SD samples, albeit at a shorter timescale. When comparing the flow stress to the GND density maps in Figure 7 as well as the predicted dislocation densities in Figure 12, it is apparent that the dislocation densities in these samples are not the main contributing factor to this increase in flow stress. As the initial grain sizes before deformation are also similar, the contribution of  $\gamma'$  precipitates to the flow requires closer attention. Dependent on local microstructure, these  $\gamma'$  precipitates can either suppress or promote recrystallization.<sup>[24,26]</sup> However, the suppression of recrystallization appears to occur more commonly due to Zener–Smith pinning, which is also expressed in increased activation energy in the presence of  $\gamma'$ .<sup>[25,27]</sup> Figure 9 does confirm the presence of distinct differences in  $\gamma'$  precipitates between the Type D and Type SD profiles, indicating this as a likely explanation for the different observations. On the other hand, process conditions favoring local  $\gamma'$  dissolution and re-precipitation may mitigate such pinning effects.<sup>[27]</sup>

The simulated and experimentally generated results can now be applied to understand the effect of  $\gamma'$  precipitates on recrystallization. This will be based on commonly used models evaluating the effect of small second phase particles on recrystallization.

### B. Modeling Recrystallization with nm-Scale $\gamma'$ Precipitates

As mentioned in the introduction, no directly applicable models are yet available to estimate the effect of small second phase particles on the recrystallization in materials where DDRX dominates. However, a model for nucleation inhibition based on Zener-limited

subgrain sizes has been put forward by Rollett *et al.*,<sup>[8]</sup> and in a similar description by Hillert.<sup>[19]</sup> This provides an estimation of limited subgrain growth due to second phase particles in volume fractions > 5 pct. It is presented here as Eq. [1a]. The model is based on the pinning pressure of small, incoherent, second phase particles and the driving force of subgrain growth due to subgrain boundary curvatures.<sup>[8]</sup>

$$\frac{F_V^{1/3}}{r} > \frac{\beta\Omega}{\Theta_m} \quad [1a]$$

Here,  $\beta$  describes a constant parameter,  $\Omega$  an orientation gradient within the microstructure, and  $\Theta_m$  the misorientation angle of a high angle grain boundary. The radius of second phase particles,  $r$ , enters the equation in units of  $\mu\text{m}$ . The value of the local orientation gradient within the deformed material  $\Omega$  is  $0.15 \text{ deg } \mu\text{m}^{-1}$ , based on point-to-origin misorientation evaluation of randomly selected lines within individual grains in the EBSD maps (see supplementary Figure S7). The high angle grain boundary misorientation  $\Theta_m$  is 15 deg as suggested by Ørsund and Nes,<sup>[20]</sup> and  $\beta$  is a numerical value of approximately 3.6, as suggested in the literature.<sup>[8,19]</sup> This allows the evaluation based on the measured and simulated  $\gamma'$  precipitate fraction and radii. For 0 seconds of isothermal holding, the simulation results in Figures 11(a) and (b) predict in the Type D profile with deformation at 1020 °C a  $\gamma'$  precipitate fraction of 5.3 mol pct and a mean volume-weighted radius of 40.5 nm. This leads to an evaluation of Eq. [1a] of:

$$\frac{0.053^{1/3}}{0.0405 \mu\text{m}} \approx 9.3 \mu\text{m}^{-1} > 0.036 \mu\text{m}^{-1} = \frac{3.6 \times 0.15^\circ \mu\text{m}^{-1}}{15^\circ} \quad [1b]$$

This equation is clearly satisfied in the present case, being consistent with the fact that almost no recrystallization is observed in Figures 4(a) and (b). When comparing this result to that of the Type D profile with deformation at 1020 °C after 360 seconds of isothermal holding, the expected volume-weighted radii of  $\gamma'$  precipitates of 42.3 nm and a slight increase of the phase fraction to 5.4 mol pct lead to a result of:

$$\frac{0.054^{1/3}}{0.0423 \mu\text{m}} \approx 8.9 \mu\text{m}^{-1} > 0.036 \mu\text{m}^{-1} = \frac{3.6 \times 0.15^\circ \mu\text{m}^{-1}}{15^\circ} \quad [1c]$$

This result indicates that no recrystallization is expected, even after isothermal holding. This contrasts with the experimental observations in Figures 4(c) and (f) and Figure 5(b). As the microstructure in this condition contains approximately 36 vol pct recrystallized material, it can be concluded that Eq. [1a] may not be applicable to superalloys.

Therefore, an alternative description of the microstructural development based on the driving forces due to Zener pinning, dislocation densities and grain/

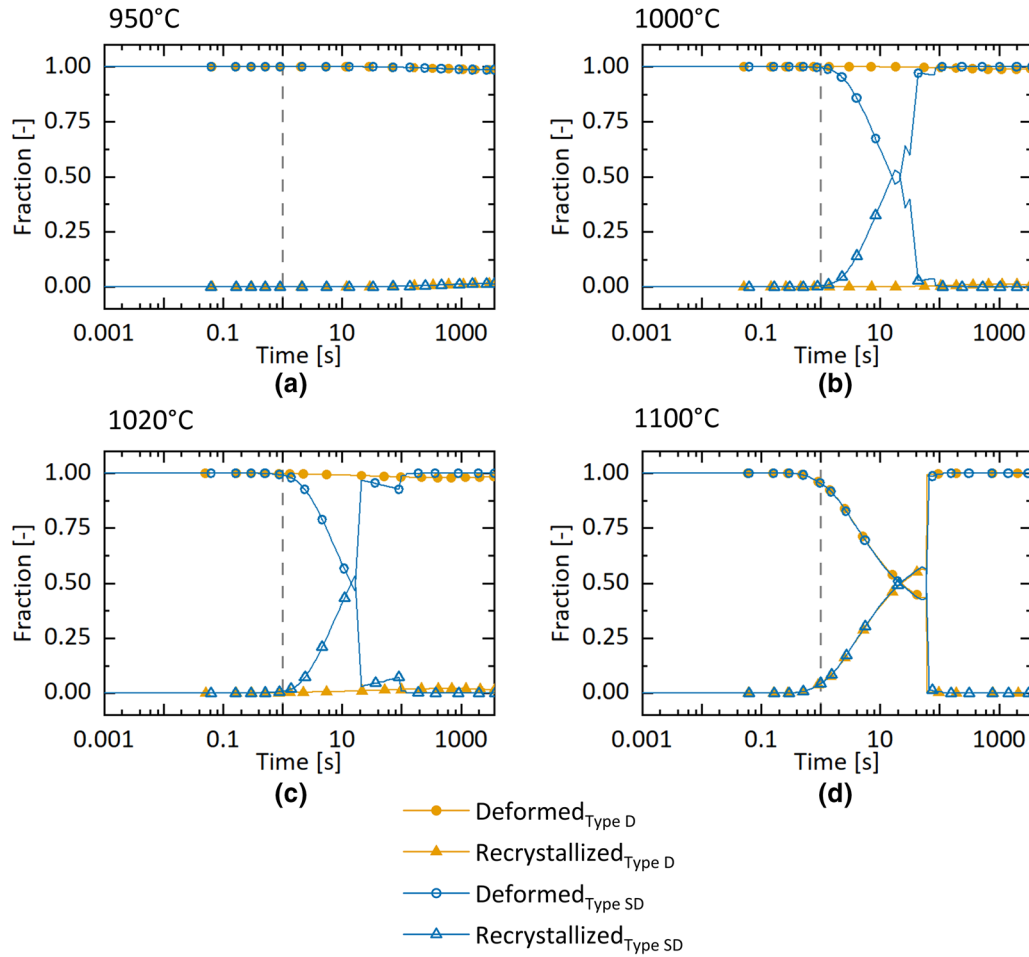


Fig. 10—MatCalc simulation of the recrystallized and deformed volume fractions during and after deformation simulations, corresponding to Type D and SD programs for temperatures of 950 °C (a), 1000 °C (b), 1020 °C (c) and 1100 °C (d). The dashed line in all plots at 1 s represents the end of plastic deformation.

nucleus curvature as applied to other deformed microstructures was attempted using in Eq. [2a], as described in Reference 8. Zener pinning is typically applied during grain growth, but may also provide information on the ability of recrystallization nuclei to grow.<sup>[8]</sup> It includes terms describing the overall driving force  $P$  for the formation of new grains due to a high dislocation density  $P_D$ , the driving force for the growth of existing grains due to grain boundary curvature  $P_R$ , as well as the Zener pinning force  $P_Z$ <sup>[8]</sup>:

$$P = P_D - P_Z - P_R$$

$$P = \alpha\rho Gb^2 - \frac{3\delta F_V\gamma_b}{2r} - \frac{2\gamma_b}{R} \quad [2a]$$

The values mainly affecting the driving forces in this equation are the radius of a recrystallization nucleus  $R$ ,  $F_V$  and  $r$  as used in Eq. [1a] and the dislocation density  $\rho$ . The numerical values  $\alpha$ , with a value of approximately  $\frac{1}{2}$ , as well as the energy of a high angle grain boundary  $\gamma_b$ , the shear modulus  $G$  and the Burgers vector  $b$  are used as constants. Commonly, the term  $\delta$  is not included in descriptions of Zener pinning, however, it was

introduced here to correct for the stronger pinning force exerted by coherent particles such as  $\gamma'$  precipitates and set to a value of 2.<sup>[17]</sup> An input value for  $\rho$  of  $1.0 \times 10^{15} \text{ m}^{-2}$  was selected.  $G$  was evaluated based on mechanical testing data and the Poisson ratio as reported in literature,<sup>[47]</sup> whereas  $\gamma_b$  was approximated using experimentally reported data for pure Ni.<sup>[52]</sup> These evaluations of  $G$  and  $\gamma_b$  at 1020 °C led to 55.9 GPa and  $0.47 \text{ J m}^{-2}$ , respectively. Based on literature,  $b$  was set to  $2.52 \text{ \AA}$ <sup>[49]</sup> and the phase fraction and radii of  $\gamma'$  precipitates were set to those matching the simulation results for a Type D profile and 0 seconds of isothermal holding as 5.3 pct and 41.1 nm as seen in Figure 11(c). These values then lead to an evaluation of Eq. [2a] of:

$$P = 1.77 \times 10^6 \text{ Pa} - 1.85 \times 10^6 \text{ Pa} - \frac{2\gamma_b}{R}$$

$$= -7.52 \times 10^4 \text{ Pa} - \frac{2\gamma_b}{R} \quad [2b]$$

As can be seen from the evaluation, the pinning force  $P_Z$  is already predicted to exceed  $P_D$ . Therefore, for any positive values of the grain boundary energy  $\gamma_b$ , no further growth of recrystallization nuclei is expected.

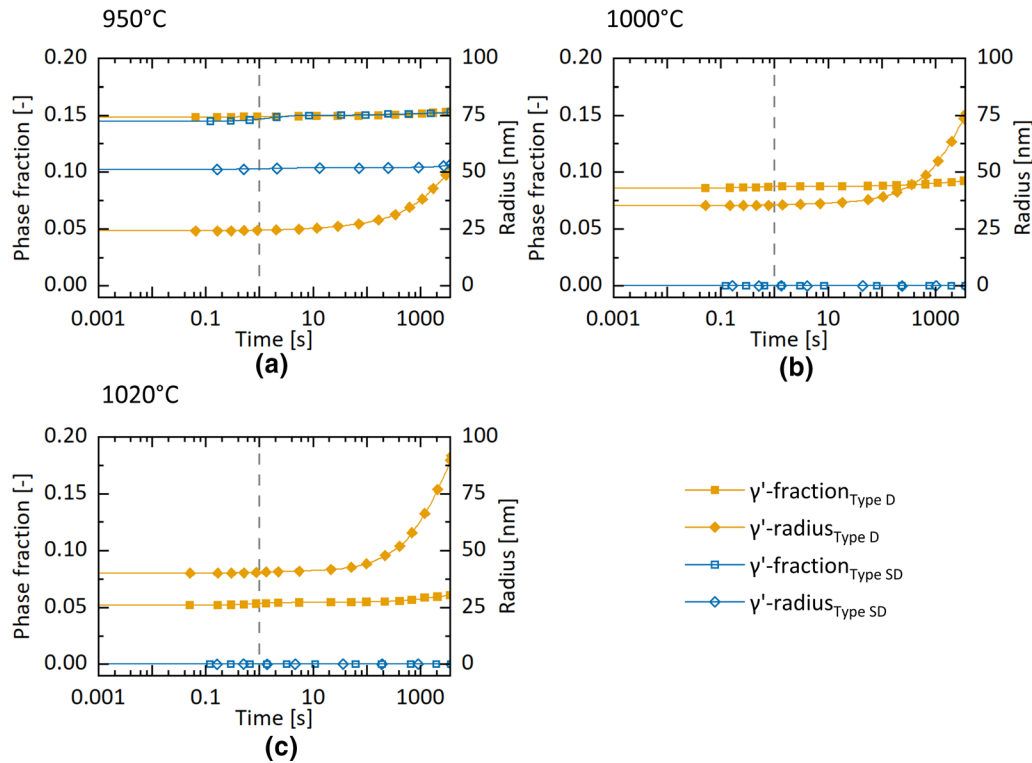


Fig. 11—MatCalc simulation predictions for the mole fraction and volume-weighted radii of  $\gamma'$  precipitates during and after deformation simulations corresponding to Type D and SD programs for temperatures of (a) 950 °C, (b) 1000 °C and (c) 1020 °C. At 1100 °C, no  $\gamma'$  precipitates were predicted during deformation, therefore these results are omitted here. The dashed line in all plots at 1 s represents the end of plastic deformation.

Using the experimentally determined grain diameters of  $3 \pm 1.7 \mu\text{m}$  seen in Figure 6(a) to evaluate the radii of recrystallized nuclei, the driving force for their growth overall equals:

$$P = -4.61 \times 10^4 \text{Pa} - 6.24 \times 10^5 \text{Pa} = -6.99 \times 10^5 \text{Pa} \quad [2c]$$

$P_Z$  is significantly larger than both  $P$  as well as the grain boundary pressure of recrystallized grains  $P_R$ . This means that the grain boundaries between the recrystallized and non-recrystallized fractions of the material are pinned in this case. Therefore, the present recrystallized grains are expected to remain stable. It should be noted that  $\gamma'$  precipitate radii are likely smaller than assumed in the simulations, as they are below the resolution limit of the SEM immediately after deformation. Only 360 seconds of isothermal holding led to sufficient coarsening, see Figure 9. It is possible that significant coarsening of the  $\gamma'$  precipitates may allow recrystallization to proceed.

Using the mean precipitate radius of 45 nm and phase fraction of 5.6 pct for  $\gamma'$  precipitates predicted in the Type D profile after 360 seconds isothermal holding as seen in Figure 11(c), Eq. [2a] yields:

$$P = 1.77 \times 10^6 \text{Pa} - 1.49 \times 10^6 \text{Pa} - \frac{2\gamma_b}{R} = +2.83 \times 10^5 \text{Pa} - \frac{2\gamma_b}{R} \quad [2d]$$

The balance between the driving force for recrystallized nuclei growth due to stored energy in the form of dislocations and Zener pinning by  $\gamma'$  precipitates is now positive. A minimum driving force for the progression of recrystallization of  $P > 0$  is required. This allows the rearrangement of [2c] into [2d] and [2e] as follows:

$$2.83 \times 10^5 \text{Pa} - \frac{2\gamma_b}{R} > 0 \quad [2e]$$

$$R > \frac{2\gamma_b}{2.83 \times 10^5 \text{Pa}} = 3.32 \mu\text{m} \quad [2f]$$

Radii exceeding this size are expected to grow further. Compared to the values for the experimentally determined diameter of  $3 \mu\text{m}$  with a standard deviation of  $1.7 \mu\text{m}$ , this is a feasible value for some of the present recrystallized grains to exceed. When comparing to Figures 6(a) and 4(c) and (f) it is apparent that there were grains satisfying this condition present in the microstructure, which then quickly grew to a diameter of approximately  $11 \mu\text{m}$ .

The driving force for the growth of grains, when the dislocation density is small as is the case in grains that were formed by recrystallization, is correlated to the inverse of the grain radius.<sup>[8]</sup> Thus, recrystallized grains that have grown to a larger size than others, have a kinetic advantage and grow rapidly into the deformed

**Table III. Molar Phase Fractions and Mean Radii of the Secondary Carbides  $M_6C$  and  $M_{23}C_6$  as Predicted by MatCalc Immediately Prior to the Deformation Simulation**

Temperature [°C]	Profile Type D				Profile Type SD			
	$M_6C$ Fraction	$M_6C$ Radius	$M_{23}C_6$ Fraction	$M_{23}C_6$ Radius	$M_6C$ Fraction	$M_6C$ Radius	$M_{23}C_6$ Fraction	$M_{23}C_6$ Radius
	[ $10^{-4}$ —]	[nm]	[ $10^{-4}$ —]	[nm]	[ $10^{-4}$ —]	[nm]	[ $10^{-4}$ —]	[nm]
950	2.1	696	16.8	870	0.4	468	1.5	449
1000	1.2	580	7.9	678	0.4	480	1.7	469
1020	1.5	622	10.3	740	0.5	485	1.8	479
1100	1.0	537	4.9	585	0.5	488	1.8	470

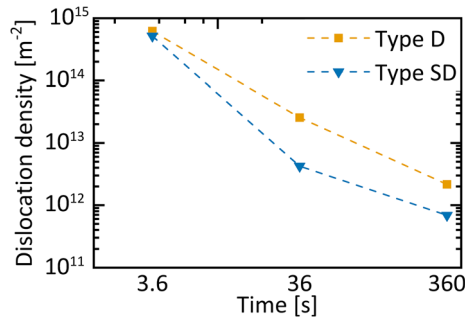


Fig. 12—Dislocation density from MatCalc simulation results for various isothermal holding periods after deformation at 1020 °C following Type D and SD heat treatments, respectively.

material. This in turn can lead to bimodal grain size distributions, as observed in Figure 5(f).

This model showed an excellent match with the observed recrystallization. It can thus be assumed, that it would also hold in similar cases in the presence of small nm-scale coherent precipitates. However, the material conditions do not include incoherent precipitates, further it is conceivable that for larger precipitates, for example in a case when the precipitate-dislocation interactions shift from cutting to Orowan-looping, this model is no longer applicable. For such different material conditions, additional investigations would be necessary, which are beyond the scope of the present study.

### C. Impact on the Design of Thermal Profiles

From these insights, several potential pathways to advancements of thermo-mechanical processing of René 41 and similar grades can be proposed. As incomplete recrystallization in superalloys is not desirable due to the tendency to abnormal grain growth,<sup>[11,53]</sup> hot deformation in a  $\gamma'$  precipitate free environment is essential for superalloys like René 41. As illustrated in Figures 4 and 6(a), the presence of  $\gamma'$  precipitates greatly affects recrystallization and recovery kinetics. In  $\gamma'$  lean microstructures, the main restoration mechanism is PDRX as shown by the EBSD datasets in Figure 5 as well as microstructural simulations in Figure 10. PDRX can also take place after deformation and isothermal holding in  $\gamma'$  containing microstructures, when the  $\gamma'$

precipitates undergo sufficient coarsening, leading to reduced Zener pinning of recrystallized grains. In either case, PDRX can result in bimodal grain size distributions reported to have detrimental effects on the mechanical properties of superalloys.<sup>[54,55]</sup> A qualitative depiction of the step-by-step evolution of the resulting microstructure can be seen in Figure 13. During the deformation from Figures 13(a) and (b) the driving force for recrystallization is provided, leading to the necklace structure in Figure 13(c). Recrystallized grains adjacent to the deformed material now have a kinetic advantage, leading to the gradual evolution to Figures 13(d) and (e). Notably, this effect occurs due to the limited number of recrystallized grains which experience the kinetic advantage. Therefore, it can be in principle compared to the effects observed by Bozzolo *et al.*,<sup>[56]</sup> who reported coarsening of the overall microstructure due to a limited number of recrystallized grains.

Bimodal structures, such as those observed here, are not desirable as a final microstructure. However, they may serve as an intermediate step during multi-step hot forging or hot rolling, as commonly applied in industrial schedules.<sup>[57–59]</sup> As such, grains formed during PDRX may provide additional nucleation sites for subsequent DDRX, allowing a better overall refinement of the microstructure.<sup>[1,2]</sup>

These insights are applicable to evaluate the current hot deformation knowledge and provide knowledge about pathways to improve hot workability of René 41. Such advances will lead to improved yield and higher formability in processing of René 41 parts but are also applicable to similar grades of Ni-based superalloys such as Waspaloy and Haynes® 282® due to similarities in precipitation kinetics and  $\gamma'$  precipitate fractions,<sup>[5,60]</sup> as well as comparable deformation responses.<sup>[3,61,62]</sup> Furthermore, a qualitative and quantitative evaluation of current recrystallization models based on experimental data is demonstrated.

## V. CONCLUSIONS

Dynamic and post-dynamic restoration processes are shown to be strongly dependent on the volume fraction and size of fine  $\gamma'$  precipitates in the Ni-based superalloy

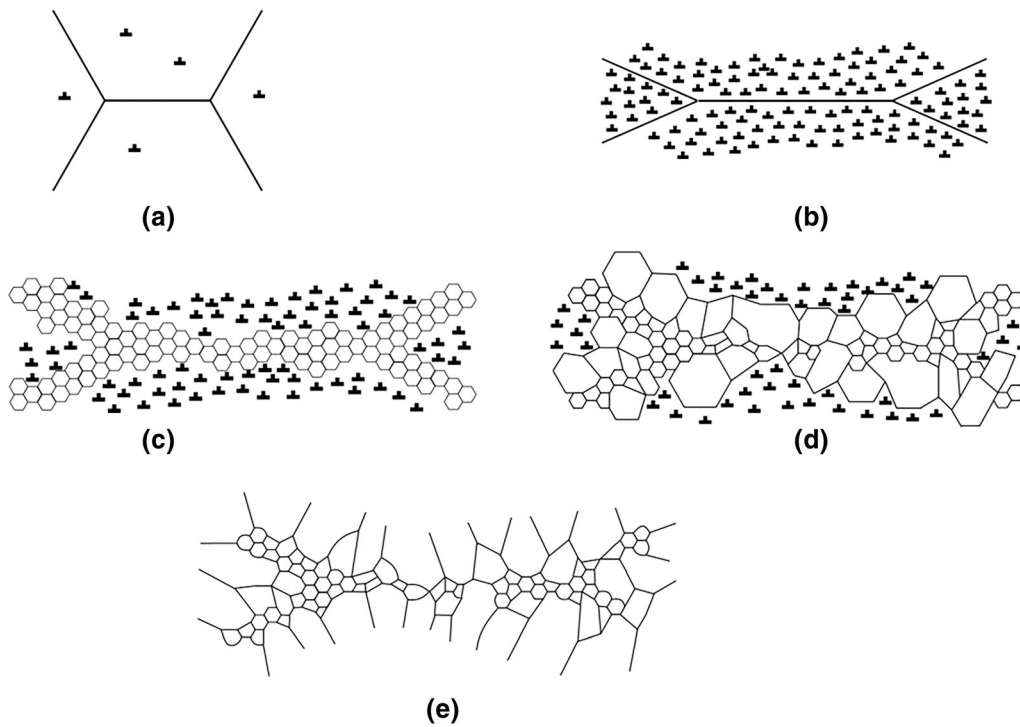


Fig. 13—(a) Undeformed coarse microstructure. (b) Deformed microstructure with high dislocation density. (c) A necklace structure forms at the previous HAGBs. (d) Some grains begin to grow at the expense of deformed material. (e) All of the deformed material is consumed by grain growth.

René 41, complicating the advancement of thermo-mechanical schedules. A model for second phase particle limited subgrain growth was found to be insufficient. Thus, a driving force model based on dislocation density, interfacial pinning by precipitates and grain boundary curvature was adapted in thermo-kinetic simulations. This adapted model led to a satisfactory match between the observed and simulated recrystallization kinetics. The same approach is expected to yield comparable results when applied to superalloys with similar  $\gamma'$  precipitate content. The main findings are summarized as follows:

- Fine  $\gamma'$  precipitate distributions stabilize the deformed microstructures and suppress recrystallization in favor of recovery.
- Solutionizing above  $\gamma'$  solvus temperature prior to hot working promotes near-complete recrystallization *via* PDRX at strain rates of  $1 \text{ s}^{-1}$ . Recrystallized grains adjacent to deformed grains experience greater kinetic advantage for growth, compared to recrystallized grains adjacent to other recrystallized grains, leading to the evolution of a coarse and bimodal microstructure.
- A model, which balances driving forces for recrystallization, grain growth and Zener pinning with nm-scale  $\gamma'$  precipitates, successfully predicts recrystallization of the  $\gamma'$ -containing superalloy René 41. This result may be applicable to other  $\gamma'$ -containing superalloys, such as Waspaloy or Haynes® 282®, allowing for an accurate prediction of the

dominating restoration mechanisms and resulting microstructural evolution in these materials. Future studies should investigate how well this model performs as precipitate size changes, as well as effects of coherent and incoherent precipitates.

- $\gamma'$  precipitation during thermo-mechanical processing must be avoided to promote recrystallisation and to enable advancements in thermo-mechanical process designs and improved control of the microstructural evolution in  $\gamma'$ -containing Ni-based superalloys. This will help to avoid potentially detrimental microstructural and mechanical properties in final products. The reduced flow stress in the  $\gamma'$  lean thermo-mechanical profiles also results in a higher ease of forming, which also translates to industrial forging processes.

## ACKNOWLEDGMENTS

This research is funded by the Australian Research Council Linkage Projects LP180100144 and LP190101169. R. Buerstmayr expresses his gratitude to Georgia and Pietro Bergamaschi for personal and financial support. The authors thank Drs. Simon Hager and Charlie Kong for technical assistance and use of facilities supported by Microscopy Australia at Electron Microscope Unit at the Mark Wainwright



Analytical Centre at UNSW. For conduction and practical assistance when executing the Gleeble compression tests the authors also thank Dr. David Misukovic from the School of Materials Science and Engineering at UNSW. R. Buerstmayr further acknowledges the contribution from the Commonwealth of Australia in the form of an Australian Government Research Training Program Scholarship.

#### AUTHOR CONTRIBUTIONS

RB: conceptualization, methodology, investigation, visualization, writing—original draft. FT: investigation, writing—review & editing. EK: software, writing—review & editing. RFW: investigation, writing—review & editing. SS: resources, writing—review & editing. ML-P: resources, writing—review & editing. SP: supervision, funding acquisition, writing—review & editing.

#### DATA AVAILABILITY

Data will be made available upon reasonable request.

#### CONFLICT OF INTEREST

The authors declare no conflict of interest.

#### FUNDING

Open Access funding enabled and organized by CAUL and its Member Institutions.

#### OPEN ACCESS

This article is licensed under a Creative Commons Attribution 4.0 International License, which permits use, sharing, adaptation, distribution and reproduction in any medium or format, as long as you give appropriate credit to the original author(s) and the source, provide a link to the Creative Commons licence, and indicate if changes were made. The images or other third party material in this article are included in the article's Creative Commons licence, unless indicated otherwise in a credit line to the material. If material is not included in the article's Creative Commons licence and your intended use is not permitted by statutory regulation or exceeds the permitted use, you will need to obtain permission directly from the copyright holder. To view a copy of this licence, visit <http://creativecommons.org/licenses/by/4.0/>.

#### SUPPLEMENTARY INFORMATION

The online version contains supplementary material available at <https://doi.org/10.1007/s11661-023-07008-w>.

#### REFERENCES

1. R.C. Reed: *The Superalloys*, Cambridge University Press, Cambridge, 2006.
2. M.J. Donachie and S.J. Donachie: *Superalloys: A Technical Guide*, 2nd ed. ASM International, Materials Park, 2002.
3. Q.L. Pan, B. Li, Y. Wang, Y.W. Zhang, and Z.M. Yin: *Mater. Sci. Eng. A*, 2013, vol. 585, pp. 371–78. <https://doi.org/10.1016/j.msea.2013.07.066>.
4. L.A. Weisenberg and R. Morris: *Met. Prog.*, 1960, vol. 78, pp. 70–74.
5. S.L. Semiatin, D.S. Weaver, R.C. Kramb, P.N. Fagin, M.G. Glavicic, R.L. Goetz, N.D. Frey, and M.M. Antony: *Metall. Mater. Trans. A*, 2004, vol. 35A, pp. 679–93. <https://doi.org/10.1007/s11661-004-0379-y>.
6. A. Nicolay, G. Fiorucci, J.M. Franchet, J. Cormier, and N. Bozzolo: *Acta Mater.*, 2019, vol. 174, pp. 406–17. <https://doi.org/10.1016/j.actamat.2019.05.061>.
7. H.K. Zhang, H. Xiao, X.W. Fang, Q. Zhang, R.E. Logé, and K. Huang: *Mater. Des.*, 2020, vol. 193, p. 108873. <https://doi.org/10.1016/j.matdes.2020.108873>.
8. A. Rollett, F.J. Humphreys, G.S. Rohrer, and M. Hatherly: *Recrystallization and Related Annealing Phenomena*, 2nd ed. Elsevier Ltd, Oxford, 2004.
9. T. Sakai, M. Ohashi, K. Chiba, and J.J. Jonas: *Acta Metall.*, 1988, vol. 36, pp. 1781–90. [https://doi.org/10.1016/0001-6160\(88\)90246-5](https://doi.org/10.1016/0001-6160(88)90246-5).
10. T. Sakai, A. Belyakov, R. Kaibyshev, H. Miura, and J.J. Jonas: *Prog. Mater. Sci.*, 2014, vol. 60, pp. 130–207. <https://doi.org/10.1016/j.pmatsci.2013.09.002>.
11. A. Agnoli, M. Bernacki, R. Logé, J.-M. Franchet, J. Laigo, and N. Bozzolo: *Superalloys*, Wiley, Hoboken, 2012, pp. 73–82.
12. L. Maire, B. Scholtes, C. Moussa, N. Bozzolo, D.P. Muñoz, A. Settefrati, and M. Bernacki: *Mater. Des.*, 2017, vol. 133, pp. 498–519. <https://doi.org/10.1016/j.matdes.2017.08.015>.
13. R.D. Doherty, D.A. Hughes, F.J. Humphreys, J.J. Jonas, D. JuulJensen, M.E. Kassner, W.E. King, T.R. McNelley, H.J. McQueen, and A.D. Rollett: *Mater. Sci. Eng. A*, 1997, vol. 238, pp. 219–74. [https://doi.org/10.1016/S0921-5093\(97\)00424-3](https://doi.org/10.1016/S0921-5093(97)00424-3).
14. H.E. Collins: *Superalloys*, 1968, pp. 171–98.
15. H.E. Collins: *ASM (Amer. Soc. Met. Trans. Quart.)*, 1969, 62, vol. 62.
16. R. Kayacan, R. Varol, and O. Kimilli: *Mater. Res. Bull.*, 2004, vol. 39, pp. 2171–86. <https://doi.org/10.1016/j.materresbull.2004.08.003>.
17. P.A. Manohar, M. Ferry, and T. Chandra: *ISIJ Int.*, 1998, vol. 38, pp. 913–24. <https://doi.org/10.2355/isijinternational.38.913>.
18. A. Rollett, F. Humphreys, G.S. Rohrer, and M. Hatherly: *Recrystallization and Related Annealing Phenomena, Chapter 9*, 2nd ed. Elsevier, Oxford, 2004.
19. M. Hillert: *Acta Metall.*, 1988, vol. 36, pp. 3177–81. [https://doi.org/10.1016/0001-6160\(88\)90053-3](https://doi.org/10.1016/0001-6160(88)90053-3).
20. R. Ørsund and E. Nes: *Scr. Metall.*, 1989, vol. 23, pp. 1187–92. [https://doi.org/10.1016/0036-9748\(89\)90324-4](https://doi.org/10.1016/0036-9748(89)90324-4).
21. K. Huang and R.E. Logé: *Mater. Des.*, 2016, vol. 111, pp. 548–74. <https://doi.org/10.1016/j.matdes.2016.09.012>.
22. R.S. Cremisio and H.J. McQueen: *Superalloys 1972 (Second Int. Symp.)*, 1972, p. G-1-G-36. [https://doi.org/10.7449/1972/Superalloys\\_1972\\_G-1\\_G-36](https://doi.org/10.7449/1972/Superalloys_1972_G-1_G-36).
23. F. Lizzi, K. Pradeep, A. Stanojevic, S. Sommadossi, and M.C. Poletti: *Metals (Basel)*, 2021, <https://doi.org/10.3390/met11040605>.
24. A. Coyne-Grell, J. Blaizot, S. Rahimi, I. Violatos, S. Nouveau, C. Dumont, A. Nicolay, and N. Bozzolo: *J. Alloys Compd.*, 2022, vol. 916, p. 165465. <https://doi.org/10.1016/j.jallcom.2022.165465>.
25. W. Zhang, X. Liu, Q. Du, H. Li, H. Qin, and Q. Tian: *J. Mater. Eng. Perform.*, 2022, <https://doi.org/10.1007/s11665-022-07320-3>.

26. T. Nishimoto, T. Okajima, Q. Zhang, J. Gong, and G. Olson: *J. Phys. Conf. Ser.*, 2019, vol. 1270, p. 012051. <https://doi.org/10.1088/1742-6596/1270/1/012051>.
27. A. Seret, C. Moussa, M. Bernacki, and N. Bozzolo: *Metall. Mater. Trans. A*, 2018, vol. 49A, pp. 4199–13. <https://doi.org/10.1007/s11661-018-4707-z>.
28. E. Kozeschnik: *Encycl. Mater. Met. Alloy.*, 2021, <https://doi.org/10.1016/B978-0-12-819726-4.00055-7>.
29. H. Buken and E. Kozeschnik: *Metall. Mater. Trans. A*, 2017, vol. 48A, pp. 2812–18. <https://doi.org/10.1007/s11661-016-3524-5>.
30. R. Ebrahimi and A. Najafzadeh: *J. Mater. Process. Technol.*, 2004, vol. 152, pp. 136–43. <https://doi.org/10.1016/j.jmatprotec.2004.03.029>.
31. D.B. Williams and C.B. Carter: *Transmission Electron Microscopy*, 2nd ed. Springer, Boston, 2009.
32. J. Schindelin, I. Arganda-Carreras, E. Frise, V. Kaynig, M. Longair, T. Pietzsch, S. Preibisch, C. Rueden, S. Saalfeld, B. Schmid, J.Y. Tinevez, D.J. White, V. Hartenstein, K. Eliceiri, P. Tomancak, and A. Cardona: *Nat. Methods*, 2012, vol. 9, pp. 676–82. <https://doi.org/10.1038/nmeth.2019>.
33. I. Arganda-Carreras, V. Kaynig, C. Rueden, K.W. Eliceiri, J. Schindelin, A. Cardona, and H.S. Seung: *Bioinformatics*, 2017, vol. 33, pp. 2424–26. <https://doi.org/10.1093/bioinformatics/btx180>.
34. I. Arganda-Carreras, V. Kaynig, C. Rueden, J. Schindelin, A. Cardona, and H.S. Seung: 2016.
35. H. Zhang, K. Zhang, H. Zhou, Z. Lu, C. Zhao, and X. Yang: *Mater. Des.*, 2015, vol. 80, pp. 51–62. <https://doi.org/10.1016/j.matdes.2015.05.004>.
36. R.K. Ham: *Philos. Mag.*, 1961, vol. 6, pp. 1183–84. <https://doi.org/10.1080/14786436108239679>.
37. E. Kozeschnik: *Modeling Solid-State Precipitation*, Momentum Press, New York, 2012.
38. [https://www.matcalc.at/images/stories/Download/Database/mc\\_n\\_i\\_v2.034.tdb](https://www.matcalc.at/images/stories/Download/Database/mc_n_i_v2.034.tdb), Accessed 1 July 2022.
39. X. Wang, H. Li, K. Chandrashekhara, S.A. Rummel, S. Lekakh, D.C. Van Aken, and R.J. O'Malley: *J. Mater. Process. Technol.*, 2017, vol. 243, pp. 465–73. <https://doi.org/10.1016/j.jmatprotec.2017.01.012>.
40. M. Bambach, I. Sizova, S. Bolz, and S. Weiß: *Metals (Basel)*, 2016, <https://doi.org/10.3390/met6090204>.
41. H. Buken, P. Sherstnev, and E. Kozeschnik: *Model. Simul. Mater. Sci. Eng.*, 2016, vol. 24, p. 035006. <https://doi.org/10.1088/0965-0393/24/3/035006>.
42. L.E. Lindgren, K. Domkin, and S. Hansson: *Mech. Mater.*, 2008, vol. 40, pp. 907–19. <https://doi.org/10.1016/j.mechmat.2008.05.005>.
43. E. Nes: *Prog. Mater. Sci.*, 1997, vol. 41, pp. 129–93. [https://doi.org/10.1016/S0079-6425\(97\)00032-7](https://doi.org/10.1016/S0079-6425(97)00032-7).
44. H. Riedel and J. Svoboda: *Mater. Sci. Eng. A*, 2016, vol. 665, pp. 175–83. <https://doi.org/10.1016/j.msea.2016.04.015>.
45. D.J. Srolovitz: No Title, <https://www.hkias.cityu.edu.hk/en/event/grain-boundary-structure-and-dynamics-a-tutorial/res=video>, (accessed 8 January 2021).
46. M.E. Kassner and M.E. McMahon: *Metall. Mater. Trans. A*, 1987, vol. 18A, pp. 835–46. <https://doi.org/10.1007/BF02646925>.
47. NiDI and INCO Ltd: *High-Temperature High-Strength Nickel Base Alloys*, 1995.
48. R.O. Simmons and R.W. Balluffi: *Phys. Rev.*, 1960, vol. 117, pp. 52–61. <https://doi.org/10.1103/PhysRev.117.52>.
49. M. Schwartz, R. Ciocoiu, D. Gheorghe, and G. Jula: *I. Ciucă*, 2015, vol. 90, pp. 95–106. <https://doi.org/10.2495/MC150091>.
50. A. Chamanfar, M. Jahazi, J. Gholipour, P. Wanjara, and S. Yue: *Mater. Sci. Eng. A*, 2014, vol. 615, pp. 497–510. <https://doi.org/10.1016/j.msea.2014.07.093>.
51. S. Utada, R. Sasaki, R.C. Reed, and Y.T. Tang: *Mater. Des.*, 2022, vol. 221, p. 110911. <https://doi.org/10.1016/j.matdes.2022.110911>.
52. T. Cheng, D. Fang, and Y. Yang: *J. Appl. Phys.*, 2018, <https://doi.org/10.1063/1.5017171>.
53. A. Agnoli, M. Bernacki, R. Logé, J.M. Franchet, J. Laigo, and N. Bozzolo: *Metall. Mater. Trans. A*, 2015, vol. 46A, pp. 4405–21. <https://doi.org/10.1007/s11661-015-3035-9>.
54. E. Eriksson and M. Hörnqvist Colliander: *Metals (Basel)*, 2021, vol. 11, pp. 1–24. <https://doi.org/10.3390/met11010122>.
55. C. Joseph, C. Persson, and M. Hörnqvist Colliander: *Mater. Sci. Eng. A*, 2017, vol. 679, pp. 520–30. <https://doi.org/10.1016/j.msea.2016.10.048>.
56. N. Bozzolo, A. Agnoli, N. Souai, M. Bernacki, and R.E. Loge: *Mater. Sci. Forum*, 2013, vol. 753, pp. 321–24. <https://doi.org/10.4028/www.scientific.net/MSF.753.321>.
57. M.C. Hardy, M. Detrois, E.T. McDevitt, C. Argyrakis, V. Saraf, P.D. Jablonski, J.A. Hawk, R.C. Buckingham, H.S. Kitaguchi, and S. Tin: *Metall. Mater. Trans. A*, 2020, vol. 51A, pp. 2626–50. <https://doi.org/10.1007/s11661-020-05773-6>.
58. S. Gardner, W. Li, M. Coleman, and R. Johnston: *Mater. Sci. Eng. A*, 2016, vol. 668, pp. 263–70. <https://doi.org/10.1016/j.msea.2016.05.051>.
59. N.K. Park, I.S. Kim, Y.S. Na, and J.T. Yeom: *J. Mater. Process. Technol.*, 2001, vol. 111, pp. 98–102. [https://doi.org/10.1016/S0924-0136\(01\)00489-7](https://doi.org/10.1016/S0924-0136(01)00489-7).
60. L.M. Pike: *Superalloys*, 2008, vol. 2008, pp. 191–200. [https://doi.org/10.7449/2008/Superalloys\\_2008\\_191\\_200](https://doi.org/10.7449/2008/Superalloys_2008_191_200).
61. A. Amiri, S. Bruschi, M.H. Sadeghi, and P. Bariani: *Mater. Sci. Eng. A*, 2013, vol. 562, pp. 77–82. <https://doi.org/10.1016/j.msea.2012.11.024>.
62. K.L. Kruger: *Materials for Ultra-Supercritical and Advanced Ultra-Supercritical Power Plants*, Elsevier, Amsterdam, 2017, pp. 511–45.

**Publisher's Note** Springer Nature remains neutral with regard to jurisdictional claims in published maps and institutional affiliations.